



Spectral analysis of turbulence kinetic and internal energy budgets in hypersonic turbulent boundary layers

Yitong Fan ^{1,2} and Weipeng Li ^{1,*}¹*School of Aeronautics and Astronautics, Shanghai Jiao Tong University, Shanghai 200240, China*²*Department of Mechanical Engineering, University of Melbourne, Parkville VIC 3010, Australia*

(Received 9 January 2023; accepted 6 April 2023; published 25 April 2023)

The evolution of turbulence kinetic and internal energy plays a critical role in aerodynamics and thermodynamics. Following the previous study on the framework of energy exchange in compressible turbulent flows [Fan *et al.*, *Phys. Rev. Fluids* 7, L092601 (2022)], we rigorously derive the spectral transport equations of turbulence kinetic and internal energy in terms of the two-point correlations of velocity and a sound-speed-like variable, respectively. With the equations, the spectral distributions of the budget terms, including production, dissipation, pressure strain, heat-conduction action, spatial and interscale transfer, are comprehensively examined in the hypersonic turbulent boundary layers at Mach number 5.86 and friction Reynolds number 420. Special attention is paid to the effect of wall cooling. The results enlighten the scale dependence of the energy transport across space and scales, and among components, helping us to clarify the evolution of turbulence kinetic and internal energy in high-speed turbulent flows.

DOI: [10.1103/PhysRevFluids.8.044604](https://doi.org/10.1103/PhysRevFluids.8.044604)

I. INTRODUCTION

The momentum transport and energy exchange in compressible turbulent boundary layers are important for aerodynamic design and thermal protection of high-speed vehicles. Due to the effects of density variation and velocity dilatation, the statistical properties and dynamical features in compressible turbulent boundary layers are more complex than those in incompressible turbulent boundary layers [1–23]. In the hypersonic regime, the wall temperature of the high-speed vehicles is usually lower than the recovery temperature of the freestream flow. A growing body of studies investigates the flow dynamics in hypersonic boundary layers over cold walls [11,24–28], showing that the mean and fluctuating fluid variables are altered not only by the variation of Mach number, but also by the strength of wall cooling. In particular, the nonmonotonic profile of mean temperature across the boundary layer invalidates the classical van Driest transformation [29], leading to a poor matching of velocity profile to its incompressible counterpart. To explicitly account for the wall heat flux, modified scaling relations and generalized Reynolds analogy have been proposed, such as Zhang *et al.* [30], Trettel and Larsson [31], Shadloo *et al.* [32], and Griffin *et al.* [33], to name a few.

When the wall temperature decreases, Duan *et al.* [11] observed enhanced compressibility effects in the turbulent boundary layers at Mach number 5, as signified via the rapid increase of turbulent and fluctuating Mach numbers. The turbulent structures, such as the near-wall streaks and hairpin vortices, tend to be more coherent with wall cooling [11,24], which may account for the increase of the skin-friction drag at the same friction Reynolds number [34]. Zhang *et al.* [25] observed that the intensity of pressure fluctuations is dramatically modulated by the wall temperature in the near-wall region but remains almost intact away from the wall. With Helmholtz decomposition, Yu

*Corresponding author: liweipeng@sjtu.edu.cn

and Xu [27] split the velocity fluctuations into solenoidal and dilatational components to quantify the effects of compressibility over cold walls. They found that as the wall temperature decreases, the dilatational components gradually dominate the vertical motions and tend to reduce the skin friction by 4%–6% in hypersonic channel flows. Xu *et al.* [28,35] investigated the influence of wall cooling on the transfer of kinetic energy in hypersonic turbulent boundary layers. They [35] stated that the wall cooling has the effect to promote the interactions between the kinetic and internal energy, which are governed by the dilatational velocity field. In addition, the wall cooling is able to enhance the local reverse transfer of kinetic energy from small- to large-scale structures while suppressing that from large to small scales [28].

In this study the major objective is to clarify the evolution processes of kinetic and internal energy in hypersonic turbulent boundary layers. To this end the approach of spectral analysis is adopted, with terms in the budget equations spectrally decomposed to reveal the scale dependence of energy exchange across space and scales, and among components [36]. In incompressible turbulent flows, where the internal energy is a constant, the spectral analysis has been well performed on the transport of turbulence kinetic energy [36–39], whereas for the compressible turbulence the spectral decomposition of turbulence kinetic energy budgets becomes more complicated due to the spatial and temporal variation of density [40]. In order to include the effect of density variation, new variables were utilized in the kinetic energy spectrum [41]. By introducing a density-weighted quantity $\omega = \sqrt{\rho}u$ (where ρ is density and u is the velocity component), Praturi and Girimaji [42] derived the spectral evolution equation for kinetic energy and examined the effect of pressure dilatation and interscale transfer in compressible turbulence. They found that the interaction between the internal and kinetic energy, associated with the pressure dilatation, causes the oscillations of the dilatational kinetic energy at large scales.

On the other hand, Clark [43] and Arun *et al.* [44] derived the transport equation of the scale-space energy density function on the basis of a mean-density-weighted two-point velocity correlation [45]. Arun *et al.* [44] investigated the effects of density variation and dilatation on the energy cascade and concluded that the production is influenced by long-distance interactions whereas the pressure dilatation is more localized in scale space. To characterize the evolution of internal energy and analyze its interaction with kinetic energy, it is feasible to manipulate the internal energy transport equation in a similar manner to that of kinetic energy. For instance, Miura and Kida [46] introduced a pressure-based variable $\Phi = \sqrt{p/(\gamma - 1)}$ (where p is pressure and γ is the specific heat ratio), so that Φ^2 directly corresponds to the internal energy. Recently, Mittal and Girimaji [40] have derived the transport equations for the mean and fluctuating components of Φ , establishing a mathematical framework to quantify the exchange and interactions between internal energy and kinetic energy. The budget terms in this pressure-based framework are found to be vanishingly small as compared to the magnitude of the kinetic contributions [35], which is ascribed to the small pressure fluctuations. In our previous work, Fan *et al.* [47] proposed to formulate the internal energy transport equation on the basis of a sound-speed-like variable (which will be introduced in Sec. II) and quantified the routes of energy exchange in hypersonic turbulent boundary layers with/without wall cooling. The formulation of the internal energy transport equation shares full structural similarity with that of the kinetic energy transport equations [47], which allows us to illuminate the connections and differences between the kinetic and internal energy. However, as for the spectral analysis of the internal energy, no further studies have been found in the open literature to date, to the best of the authors' knowledge.

In this study we aim to perform a systematic and in-depth spectral analysis of the turbulence kinetic and internal energy budgets in the hypersonic turbulent boundary layers, with special attention paid to the effects of wall temperature. This paper is outlined as follows. In Sec. II we derive the transport equations for the two-point correlations of velocity and a sound-speed-like variable, which yield the spectral decomposition of the turbulence kinetic energy and turbulence internal energy budget equation. Direct numerical simulations of three spatially developing zero-pressure-gradient hypersonic turbulent boundary layers are described in Sec. III. In Secs. IV and V, the spectral

analysis of the budgets is conducted to reveal the evolution of turbulence kinetic and internal energy, respectively. Finally, concluding remarks are given in Sec. VI.

II. TRANSPORT EQUATIONS

A. Transport equation for the two-point correlation of velocity

By applying Reynolds decomposition to the Navier-Stokes equations, we can get two forms of equations for the velocity fluctuations [44],

$$\begin{aligned} \frac{\partial u_i''}{\partial t} + u_k'' \frac{\partial u_i''}{\partial x_k} + \{u_k\} \frac{\partial u_i''}{\partial x_k} + u_k'' \frac{\partial \{u_i\}}{\partial x_k} - \frac{1}{\langle \rho \rangle} \frac{\partial \langle \rho u_k'' u_i'' \rangle}{\partial x_k} \\ = \frac{1}{\rho} \frac{\partial \sigma'_{ik}}{\partial x_k} - \left(\frac{1}{\langle \rho \rangle} - \frac{1}{\rho} \right) \frac{\partial \langle \sigma_{ik} \rangle}{\partial x_k}, \end{aligned} \quad (1)$$

$$\begin{aligned} \frac{\partial \rho u_i''}{\partial t} + \frac{\partial \rho u_k'' u_i''}{\partial x_k} + \frac{\partial \rho \{u_k\} u_i''}{\partial x_k} + \rho u_k'' \frac{\partial \{u_i\}}{\partial x_k} - \frac{\rho}{\langle \rho \rangle} \frac{\partial \langle \rho u_k'' u_i'' \rangle}{\partial x_k} \\ = \frac{\partial \sigma'_{ik}}{\partial x_k} - \left(\frac{\rho}{\langle \rho \rangle} - 1 \right) \frac{\partial \langle \sigma_{ik} \rangle}{\partial x_k}, \end{aligned} \quad (2)$$

where $\langle \cdot \rangle$ and $\{ \cdot \}$ are the Reynolds- and Favre-averaging operators, respectively, and the single and double prime represent the turbulent fluctuations with respect to the Reynolds and Favre average, respectively. t is time, ρ is density, x_k ($k = 1, 2, 3$) denotes the streamwise, wall-normal and spanwise direction, respectively, and u_k denotes the corresponding velocity components. $\sigma_{ij} = -p\delta_{ij} + \tau_{ij}$, where p is pressure, δ_{ij} is the Kronecker delta, τ_{ij} is the viscous stress calculated by $\mu[(\partial u_i/\partial x_j + \partial u_j/\partial x_i) - \frac{2}{3}\delta_{ij}\partial u_k/\partial x_k]$, and μ is the dynamic viscosity.

Considering two points at (x_1, x_2, x_3) and $(\tilde{x}_1, \tilde{x}_2, \tilde{x}_3)$, a generalized velocity correlation in the compressible flows is defined as [45]

$$R_{\rho u_i u_j} = \left\langle \frac{1}{2}(\rho + \tilde{\rho}) u_i'' \tilde{u}_j'' \right\rangle, \quad (3)$$

where the superscript $\tilde{\cdot}$ denotes the variable at $(\tilde{x}_1, \tilde{x}_2, \tilde{x}_3)$. The time derivative of $R_{\rho u_i u_j}$ is expressed as

$$\frac{\partial R_{\rho u_i u_j}}{\partial t} = \frac{1}{2} \left\langle \rho u_i'' \frac{\partial \tilde{u}_j''}{\partial t} \right\rangle + \frac{1}{2} \left\langle \tilde{u}_j'' \frac{\partial \rho u_i''}{\partial t} \right\rangle + \frac{1}{2} \left\langle \tilde{\rho} \tilde{u}_j'' \frac{\partial u_i''}{\partial t} \right\rangle + \frac{1}{2} \left\langle u_i'' \frac{\partial \tilde{\rho} \tilde{u}_j''}{\partial t} \right\rangle. \quad (4)$$

Substituting (1) and (2) into (4), we can obtain the transport equation for the two-point correlation tensor $R_{\rho u_i u_j}$ (see more details in Arun *et al.* [44]):

$$\frac{\partial R_{\rho u_i u_j}}{\partial t} = R_{\rho u_i u_j}^{P_k} - R_{\rho u_i u_j}^{E_k} + R_{\rho u_i u_j}^{\Pi p} + R_{\rho u_i u_j}^{D_p} + R_{\rho u_i u_j}^{D_v} + R_{\rho u_i u_j}^{D_t} + R_{\rho u_i u_j}^C + R_{\rho u_i u_j}^M. \quad (5)$$

The right-hand terms in (5) are expressed as

$$R_{\rho u_i u_j}^{P_k} = -\frac{1}{2} \left(\left\langle (\rho + \tilde{\rho}) u_k'' \tilde{u}_j'' \frac{\partial \{u_i\}}{\partial x_k} \right\rangle + \left\langle (\rho + \tilde{\rho}) u_i'' \tilde{u}_k'' \frac{\partial \{u_j\}}{\partial \tilde{x}_k} \right\rangle \right), \quad (6a)$$

$$R_{\rho u_i u_j}^{E_k} = \frac{1}{2} \left(\left\langle \left(1 + \frac{\tilde{\rho}}{\rho} \right) \tau'_{ik} \frac{\partial \tilde{u}_j''}{\partial x_k} \right\rangle + \left\langle \left(1 + \frac{\rho}{\tilde{\rho}} \right) \tilde{\tau}'_{jk} \frac{\partial u_i''}{\partial \tilde{x}_k} \right\rangle \right), \quad (6b)$$

$$R_{\rho u_i u_j}^{\Pi p} = \frac{1}{2} \left(\left\langle \left(1 + \frac{\tilde{\rho}}{\rho} \right) p' \frac{\partial \tilde{u}_j''}{\partial x_i} \right\rangle + \left\langle \left(1 + \frac{\rho}{\tilde{\rho}} \right) \tilde{p}' \frac{\partial u_i''}{\partial \tilde{x}_j} \right\rangle \right), \quad (6c)$$

$$R_{\rho u_i u_j}^{D_p} = -\frac{1}{2} \left(\left\langle \left(1 + \frac{\tilde{\rho}}{\rho} \right) \frac{\partial p' \tilde{u}_j''}{\partial x_i} \right\rangle + \left\langle \left(1 + \frac{\rho}{\tilde{\rho}} \right) \frac{\partial \tilde{p}' u_i''}{\partial \tilde{x}_j} \right\rangle \right), \quad (6d)$$

$$R_{\rho u_i u_j}^{D_v} = \frac{1}{2} \left(\left\langle \left(1 + \frac{\tilde{\rho}}{\rho} \right) \frac{\partial \tau'_{ik} \tilde{u}''_j}{\partial x_k} \right\rangle + \left\langle \left(1 + \frac{\rho}{\tilde{\rho}} \right) \frac{\partial \tilde{\tau}'_{jk} u''_i}{\partial \tilde{x}_k} \right\rangle \right), \quad (6e)$$

$$R_{\rho u_i u_j}^{D_t} = -\frac{1}{2} \left(\left\langle \tilde{\rho} \tilde{u}''_j u''_k \frac{\partial u''_i}{\partial x_k} + \tilde{u}''_j \frac{\partial \rho u''_i u''_k}{\partial x_k} \right\rangle + \left\langle \rho u''_i u''_k \frac{\partial \tilde{u}''_j}{\partial \tilde{x}_k} + u''_i \frac{\partial \tilde{\rho} \tilde{u}''_j \tilde{u}''_k}{\partial \tilde{x}_k} \right\rangle \right), \quad (6f)$$

$$R_{\rho u_i u_j}^C = -\frac{1}{2} \left\langle \tilde{\rho} \tilde{u}''_j \{u_k\} \frac{\partial u''_i}{\partial x_k} + \tilde{u}''_j \frac{\partial \rho u''_i \{u_k\}}{\partial x_k} + \rho u''_i \{\tilde{u}_k\} \frac{\partial \tilde{u}''_j}{\partial \tilde{x}_k} + u''_i \frac{\partial \tilde{\rho} \tilde{u}''_j \{\tilde{u}_k\}}{\partial \tilde{x}_k} \right\rangle, \quad (6g)$$

$$\begin{aligned} R_{\rho u_i u_j}^M &= \frac{1}{2} \left(\left\langle \frac{\rho u''_i}{\tilde{\rho}} \right\rangle + \langle u''_i \rangle - \frac{\langle \tilde{\rho} u''_i \rangle}{\langle \tilde{\rho} \rangle} \right) \left(-\frac{\partial \langle \tilde{p} \rangle}{\partial \tilde{x}_j} + \frac{\partial \langle \tilde{\tau}_{jk} \rangle}{\partial \tilde{x}_k} \right) \\ &\quad + \frac{1}{2} \left(\left\langle \frac{\tilde{\rho} \tilde{u}''_j}{\rho} \right\rangle + \langle \tilde{u}''_j \rangle - \frac{\langle \rho \tilde{u}''_j \rangle}{\langle \rho \rangle} \right) \left(-\frac{\partial \langle p \rangle}{\partial x_i} + \frac{\partial \langle \tau_{ik} \rangle}{\partial x_k} \right) \\ &\quad + \frac{1}{2} \left(\frac{\langle \rho \tilde{u}''_j \rangle}{\langle \rho \rangle} \frac{\partial \langle \rho u''_i u''_k \rangle}{\partial x_k} + \frac{\langle \tilde{\rho} u''_i \rangle}{\langle \tilde{\rho} \rangle} \frac{\partial \langle \tilde{\rho} \tilde{u}''_j \tilde{u}''_k \rangle}{\partial \tilde{x}_k} \right), \end{aligned} \quad (6h)$$

where $R_{\rho u_i u_j}^{D_k}$ is interpreted as the production term, $R_{\rho u_i u_j}^{E_k}$ accounts for the viscous dissipation, $R_{\rho u_i u_j}^{PP}$ for the pressure strain, $R_{\rho u_i u_j}^{D_p}$ and $R_{\rho u_i u_j}^{D_v}$ account for the pressure and viscous diffusion, respectively, $R_{\rho u_i u_j}^{D_t}$ for the turbulent convection, $R_{\rho u_i u_j}^C$ for the mean-flow convection, and $R_{\rho u_i u_j}^M$ is associated with the effect of density variation.

For the turbulent boundary layers under scrutiny, we do not consider the two-point correlation in the wall-normal direction, assuming $x_2 = \tilde{x}_2$. The streamwise and spanwise separation are defined as $r_x = \tilde{x}_1 - x_1$ and $r_z = \tilde{x}_3 - x_3$, respectively. Then the term of turbulent convection ($R_{\rho u_i u_j}^{D_t}$) can be further decomposed into energy transport in the spatial direction and across scales, viz.

$$R_{\rho u_i u_j}^{D_t} = R_{\rho u_i u_j}^{D_{t,x}} + R_{\rho u_i u_j}^{D_{t,\perp}} + R_{\rho u_i u_j}^{D_{t,\parallel}}, \quad (7)$$

where $R_{\rho u_i u_j}^{D_{t,x}}$ represents the effect of streamwise heterogeneity, $R_{\rho u_i u_j}^{D_{t,\perp}}$ denotes the transport of $R_{\rho u_i u_j}$ in the wall-normal direction, and $R_{\rho u_i u_j}^{D_{t,\parallel}}$ denotes the transport across scales. Note that $R_{\rho u_i u_j}^{D_{t,x}}$ is not considered in channels as the streamwise homogeneity is assumed [36]. The latter two contributions in (7) satisfy

$$\int_0^\infty R_{\rho u_i u_j}^{D_{t,\perp}} dy = 0, \quad \forall (r_x, r_z), \quad (8a)$$

$$\lim_{(r_x, r_z) \rightarrow (0,0)} R_{\rho u_i u_j}^{D_{t,\parallel}} = 0, \quad \forall y. \quad (8b)$$

Hereafter, as a matter of convenience, we also use x , y , and z to represent the streamwise, wall-normal, and spanwise direction, respectively, and use u , v , and w to represent the corresponding velocities. Then the three terms on the right-hand side of (7) are formulated as

$$R_{\rho u_i u_j}^{D_{t,x}} = -\frac{1}{2} \frac{\langle r_{\rho u_i u_j} u'' \rangle}{\partial X} - \frac{1}{2} \frac{\langle r_{\rho u_i u_j} \tilde{u}'' \rangle}{\partial X}, \quad (9a)$$

$$R_{\rho u_i u_j}^{D_{t,\perp}} = -\frac{1}{2} \frac{\partial \langle r_{\rho u_i u_j} v'' \rangle}{\partial y} - \frac{1}{2} \frac{\partial \langle r_{\rho u_i u_j} \tilde{v}'' \rangle}{\partial y}, \quad (9b)$$

$$\begin{aligned}
 R_{\rho u_i u_j}^{D_{r,\parallel}} &= \frac{\partial \langle r_{\rho u_i u_j} u'' \rangle}{\partial r_x} - \frac{\partial \langle r_{\rho u_i u_j} \tilde{u}'' \rangle}{\partial r_x} + \frac{\partial \langle r_{\rho u_i u_j} w'' \rangle}{\partial r_z} - \frac{\partial \langle r_{\rho u_i u_j} \tilde{w}'' \rangle}{\partial r_z} \\
 &+ \frac{1}{2} \left(\left\langle u_i'' v'' \frac{\partial \tilde{\rho} \tilde{u}_j''}{\partial y} + \rho u_i'' v'' \frac{\partial \tilde{u}_j''}{\partial y} \right\rangle + \left\langle \tilde{u}_j'' \tilde{v}'' \frac{\partial \rho u_i''}{\partial y} + \tilde{\rho} \tilde{u}_j'' \tilde{v}'' \frac{\partial u_i''}{\partial y} \right\rangle \right) \\
 &- \frac{1}{2} \frac{\partial \langle r_{\rho u_i u_j} v'' \rangle}{\partial y} - \frac{1}{2} \frac{\partial \langle r_{\rho u_i u_j} \tilde{v}'' \rangle}{\partial y} + \frac{1}{2} \left\langle \tilde{\rho} \tilde{u}_j'' u_i'' \frac{\partial u_k''}{\partial x_k} + \rho u_i'' \tilde{u}_j'' \frac{\partial \tilde{u}_k''}{\partial \tilde{x}_k} \right\rangle, \quad (9c)
 \end{aligned}$$

where $r_{\rho u_i u_j} = \frac{1}{2}(\rho + \tilde{\rho})u_i''\tilde{u}_j''$ and $X = (x + \tilde{x})/2$.

Lastly, substituting (7) into (5) and taking the Fourier transform, we can get the evolution equation of $R_{\rho u_i u_j}$ in the frequency domain:

$$\begin{aligned}
 \frac{\partial E_{\rho u_i u_j}}{\partial t} &= E_{\rho u_i u_j}^{P_k} - E_{\rho u_i u_j}^{\varepsilon_k} + E_{\rho u_i u_j}^{P^p} + E_{\rho u_i u_j}^{D_p} + E_{\rho u_i u_j}^{D_v} + E_{\rho u_i u_j}^{D_{r,\perp}} \\
 &+ E_{\rho u_i u_j}^{D_{r,\parallel}} + E_{\rho u_i u_j}^{D_{r,x}} + E_{\rho u_i u_j}^C + E_{\rho u_i u_j}^M, \quad (10)
 \end{aligned}$$

with $\lim_{(r_x, r_z) \rightarrow (0,0)} R_{\rho u_i u_j}(r_x, y, r_z) = \iint E_{\rho u_i u_j}(k_x, y, k_z) dk_x dk_z$, where k_x and k_z are the streamwise and spanwise wave number, respectively. Terms in Eq. (10) are reminiscent of the Reynolds stress budgets, and it can be regarded as a spectral decomposition of the Reynolds stress transport equation (except for $E_{\rho u_i u_j}^{D_{r,\parallel}}$). In this paper we will only consider the three diagonal elements in the Reynolds stress tensor (turbulence kinetic energy) and investigate the scale dependence of the turbulence-kinetic-energy evolution.

B. Transport equation for the two-point correlation of a sound-speed-like variable

A sound-speed-like variable ϕ [47] is utilized to derive the governing equations of turbulence internal energy. The sound-speed-like variable ϕ is expressed as

$$\phi = \sqrt{C_v T} = \frac{c}{[(\gamma - 1)\gamma]^{1/2}}, \quad (11)$$

where C_v is the specific heat at constant volume, T is temperature, c is the speed of sound, and γ is the specific heat ratio. With this definition the internal energy becomes $e = \rho\phi^2$, which is straightforwardly analogized to the expression of kinetic energy, $k = 1/2\rho u_i^2$, allowing similarities and differences of the energy evolution between the kinetic energy and internal energy to be discovered [47].

With (11), the energy equation in the Navier-Stokes equations is reformulated as

$$\frac{\partial \rho\phi^2}{\partial t} + \frac{\partial \rho\phi^2 u_k}{\partial x_k} = -\frac{\partial q_k}{\partial x_k} - p \frac{\partial u_k}{\partial x_k} + \tau_{ij} \frac{\partial u_i}{\partial x_j}, \quad (12)$$

where q_k is the heat conduction calculated by $q_k = -K\partial T/\partial x_k$ and K is the thermal conductivity coefficient. For brevity, let $f = -\partial q_k/\partial x_k - p\partial u_k/\partial x_k + \tau_{ij}\partial u_i/\partial x_j$. Applying Reynolds decomposition to (12), we obtain the primitive and conservative form of the fluctuating ϕ equations, respectively, as

$$\frac{\partial \phi''}{\partial t} + u_k'' \frac{\partial \phi''}{\partial x_k} + \{u_k\} \frac{\partial \phi''}{\partial x_k} + u_k'' \frac{\partial \{\phi\}}{\partial x_k} - \frac{1}{\langle \rho \rangle} \frac{\partial \langle \rho u_k'' \phi'' \rangle}{\partial x_k} = \frac{1}{\rho} \left(\frac{f}{2\phi} \right)' - \left(\frac{1}{\langle \rho \rangle} - \frac{1}{\rho} \right) \left\langle \frac{f}{2\phi} \right\rangle, \quad (13)$$

$$\frac{\partial \rho\phi''}{\partial t} + \frac{\partial \rho u_k'' \phi''}{\partial x_k} + \frac{\partial \rho \{u_k\} \phi''}{\partial x_k} + \rho u_k'' \frac{\partial \{\phi\}}{\partial x_k} - \frac{\rho}{\langle \rho \rangle} \frac{\partial \langle \rho u_k'' \phi'' \rangle}{\partial x_k} = \left(\frac{f}{2\phi} \right)' - \left(\frac{\rho}{\langle \rho \rangle} - 1 \right) \left\langle \frac{f}{2\phi} \right\rangle. \quad (14)$$

Similar to (3), we define the two-point correlation of ϕ'' as

$$R_{\rho\phi\phi} = \left\langle \frac{1}{2}(\rho + \tilde{\rho})\phi''\tilde{\phi}'' \right\rangle. \quad (15)$$

The time derivative of $R_{\rho\phi\phi}$ also incorporates four terms, i.e., $\tilde{\rho}\tilde{\phi}''\partial\phi''/\partial t$, $\rho\phi''\partial\tilde{\phi}''/\partial t$, $\tilde{\phi}''\partial\rho\phi''/\partial t$, and $\phi''\partial\tilde{\rho}\tilde{\phi}''/\partial t$, which can be obtained on the basis of (13) and (14):

$$\begin{aligned} \tilde{\rho}\tilde{\phi}''\frac{\partial\phi''}{\partial t} &= -\tilde{\rho}\tilde{\phi}''u_k''\frac{\partial\phi''}{\partial x_k} - \tilde{\rho}\tilde{\phi}''\{u_k\}\frac{\partial\phi''}{\partial x_k} - \tilde{\rho}\tilde{\phi}''u_k''\frac{\partial\{\phi\}}{\partial x_k} + \frac{\tilde{\rho}\tilde{\phi}''}{\langle\rho\rangle}\frac{\partial\langle\rho u_k''\phi''\rangle}{\partial x_k} \\ &\quad + \frac{\tilde{\rho}\tilde{\phi}''}{\rho}\left(\frac{f}{2\phi}\right)' - \left(\frac{1}{\langle\rho\rangle} - \frac{1}{\rho}\right)\tilde{\rho}\tilde{\phi}''\left\langle\frac{f}{2\phi}\right\rangle, \end{aligned} \quad (16a)$$

$$\begin{aligned} \rho\phi''\frac{\partial\tilde{\phi}''}{\partial t} &= -\rho\phi''\tilde{u}_k''\frac{\partial\tilde{\phi}''}{\partial \tilde{x}_k} - \rho\phi''\{\tilde{u}_k\}\frac{\partial\tilde{\phi}''}{\partial \tilde{x}_k} - \rho\phi''\tilde{u}_k''\frac{\partial\{\tilde{\phi}\}}{\partial \tilde{x}_k} + \frac{\rho\phi''}{\langle\tilde{\rho}\rangle}\frac{\partial\langle\tilde{\rho}\tilde{u}_k''\tilde{\phi}''\rangle}{\partial \tilde{x}_k} \\ &\quad + \frac{\rho\phi''}{\tilde{\rho}}\left(\frac{\tilde{f}}{2\tilde{\phi}}\right)' - \left(\frac{1}{\langle\tilde{\rho}\rangle} - \frac{1}{\tilde{\rho}}\right)\rho\phi''\left\langle\frac{\tilde{f}}{2\tilde{\phi}}\right\rangle, \end{aligned} \quad (16b)$$

$$\begin{aligned} \tilde{\phi}''\frac{\partial\rho\phi''}{\partial t} &= -\tilde{\phi}''\frac{\partial\rho u_k''\phi''}{\partial x_k} - \tilde{\phi}''\frac{\partial\rho\{u_k\}\phi''}{\partial x_k} - \tilde{\phi}''\rho u_k''\frac{\partial\{\phi\}}{\partial x_k} + \frac{\rho\tilde{\phi}''}{\langle\rho\rangle}\frac{\partial\langle\rho u_k''\phi''\rangle}{\partial x_k} \\ &\quad + \tilde{\phi}''\left(\frac{f}{2\phi}\right)' - \left(\frac{\rho}{\langle\rho\rangle} - 1\right)\tilde{\phi}''\left\langle\frac{f}{2\phi}\right\rangle, \end{aligned} \quad (16c)$$

$$\begin{aligned} \phi''\frac{\partial\tilde{\rho}\tilde{\phi}''}{\partial t} &= -\phi''\frac{\partial\tilde{\rho}\tilde{u}_k''\tilde{\phi}''}{\partial \tilde{x}_k} - \phi''\frac{\partial\tilde{\rho}\{\tilde{u}_k\}\tilde{\phi}''}{\partial \tilde{x}_k} - \phi''\tilde{\rho}\tilde{u}_k''\frac{\partial\{\tilde{\phi}\}}{\partial \tilde{x}_k} + \frac{\tilde{\rho}\phi''}{\langle\tilde{\rho}\rangle}\frac{\partial\langle\tilde{\rho}\tilde{u}_k''\tilde{\phi}''\rangle}{\partial \tilde{x}_k} \\ &\quad + \phi''\left(\frac{\tilde{f}}{2\tilde{\phi}}\right)' - \left(\frac{\tilde{\rho}}{\langle\tilde{\rho}\rangle} - 1\right)\phi''\left\langle\frac{\tilde{f}}{2\tilde{\phi}}\right\rangle. \end{aligned} \quad (16d)$$

Consequently, we can get the transport equation of $R_{\rho\phi\phi}$,

$$\frac{\partial R_{\rho\phi\phi}}{\partial t} = R_{\rho\phi\phi}^{P_e} + R_{\rho\phi\phi}^Q + R_{\rho\phi\phi}^{pw} + R_{\rho\phi\phi}^{vw} + R_{\rho\phi\phi}^{D_t} + R_{\rho\phi\phi}^C + R_{\rho\phi\phi}^M, \quad (17)$$

where $R_{\rho\phi\phi}^{P_e}$ represents the production of the two-point correlation of ϕ'' , $R_{\rho\phi\phi}^{D_t}$ denotes the turbulent convection, $R_{\rho\phi\phi}^Q$, $R_{\rho\phi\phi}^{pw}$, and $R_{\rho\phi\phi}^{vw}$ are the contributions of heat conduction, pressure work, and viscous work, respectively, $R_{\rho\phi\phi}^C$ is the mean-flow convection, and $R_{\rho\phi\phi}^M$ is associated with the effect of temperature variation.

The terms in (17) are formulated as

$$R_{\rho\phi\phi}^{P_e} = -\frac{1}{2}\left(\langle(\rho + \tilde{\rho})\tilde{\phi}''u_k''\rangle\frac{\partial\{\phi\}}{\partial x_k} + \langle(\rho + \tilde{\rho})\phi''\tilde{u}_k''\rangle\frac{\partial\{\tilde{\phi}\}}{\partial \tilde{x}_k}\right), \quad (18a)$$

$$R_{\rho\phi\phi}^Q = -\frac{1}{2}\left(\left\langle\left(\frac{\tilde{\rho}}{\rho} + 1\right)\tilde{\phi}''\left(\frac{\partial q_k/\partial x_k}{2\phi}\right)\right\rangle + \left\langle\left(\frac{\rho}{\tilde{\rho}} + 1\right)\phi''\left(\frac{\partial \tilde{q}_k/\partial \tilde{x}_k}{2\tilde{\phi}}\right)\right\rangle\right), \quad (18b)$$

$$R_{\rho\phi\phi}^{pw} = -\frac{1}{2}\left(\left\langle\left(\frac{\tilde{\rho}}{\rho} + 1\right)\tilde{\phi}''\left(\frac{p\partial u_k/\partial x_k}{2\phi}\right)\right\rangle + \left\langle\left(\frac{\rho}{\tilde{\rho}} + 1\right)\phi''\left(\frac{\tilde{p}\partial \tilde{u}_k/\partial \tilde{x}_k}{2\tilde{\phi}}\right)\right\rangle\right), \quad (18c)$$

$$R_{\rho\phi\phi}^{vw} = \frac{1}{2}\left(\left\langle\left(\frac{\tilde{\rho}}{\rho} + 1\right)\tilde{\phi}''\left(\frac{\tau_{ij}\partial u_i/\partial x_j}{2\phi}\right)\right\rangle + \left\langle\left(\frac{\rho}{\tilde{\rho}} + 1\right)\phi''\left(\frac{\tilde{\tau}_{ij}\partial \tilde{u}_i/\partial \tilde{x}_j}{2\tilde{\phi}}\right)\right\rangle\right), \quad (18d)$$

$$R_{\rho\phi\phi}^{D_t} = -\frac{1}{2}\left(\left\langle\tilde{\rho}\tilde{\phi}''u_k''\frac{\partial\phi''}{\partial x_k} + \tilde{\phi}''\frac{\partial\rho u_k''\phi''}{\partial x_k}\right\rangle + \left\langle\rho\phi''\tilde{u}_k''\frac{\partial\tilde{\phi}''}{\partial \tilde{x}_k} + \phi''\frac{\partial\tilde{\rho}\tilde{u}_k''\tilde{\phi}''}{\partial \tilde{x}_k}\right\rangle\right), \quad (18e)$$

$$R_{\rho\phi\phi}^C = -\frac{1}{2}\left\langle\tilde{\rho}\tilde{\phi}''\phi''\frac{\partial\{u_k\}}{\partial x_k} + \tilde{\phi}''\frac{\partial\rho\{u_k\}\phi''}{\partial x_k} + \rho\phi''\tilde{\phi}''\frac{\partial\{\tilde{u}_k\}}{\partial \tilde{x}_k} + \phi''\frac{\partial\tilde{\rho}\{\tilde{u}_k\}\tilde{\phi}''}{\partial \tilde{x}_k}\right\rangle, \quad (18f)$$

$$R_{\rho\phi\phi}^M = -\frac{1}{2}\left(\left\langle\frac{\rho\tilde{\phi}''}{\langle\rho\rangle}\left\langle\frac{f}{2\phi} - \frac{\langle\rho u_k''\phi''\rangle}{\partial x_k}\right\rangle + \frac{\langle\tilde{\rho}\phi''\rangle}{\langle\tilde{\rho}\rangle}\left\langle\frac{\tilde{f}}{2\tilde{\phi}} - \frac{\langle\tilde{\rho}\tilde{u}_k''\tilde{\phi}''\rangle}{\partial \tilde{x}_k}\right\rangle\right), \quad (18g)$$

Similar to the decomposition of $R_{\rho u_i u_j}^{D_t}$, the turbulent convection of $R_{\rho\phi\phi}^{D_t}$ is also decomposed into three parts:

$$R_{\rho\phi\phi}^{D_t} = R_{\rho\phi\phi}^{D_{t,x}} + R_{\rho\phi\phi}^{D_{t,\perp}} + R_{\rho\phi\phi}^{D_{t,\parallel}}, \quad (19)$$

where $R_{\rho\phi\phi}^{D_{t,x}}$ represents the effect of streamwise heterogeneity, $R_{\rho\phi\phi}^{D_{t,\perp}}$ denotes the transport of $R_{\rho\phi\phi}$ in the wall-normal direction, and $R_{\rho\phi\phi}^{D_{t,\parallel}}$ denotes the transport across scales. The $R_{\rho\phi\phi}^{D_{t,\perp}}$ and $R_{\rho\phi\phi}^{D_{t,\parallel}}$ satisfy

$$\int_0^\infty R_{\rho\phi\phi}^{D_{t,\perp}} dy = 0, \quad \forall(r_x, r_z), \quad (20a)$$

$$\lim_{(r_x, r_z) \rightarrow (0,0)} R_{\rho\phi\phi}^{D_{t,\parallel}} = 0, \quad \forall y. \quad (20b)$$

The three components in (19) are formulated as

$$R_{\rho\phi\phi}^{D_{t,x}} = -\frac{1}{2} \frac{\langle r_{\rho\phi\phi} u'' \rangle}{\partial X} - \frac{1}{2} \frac{\langle r_{\rho\phi\phi} \tilde{u}'' \rangle}{\partial X}, \quad (21a)$$

$$R_{\rho\phi\phi}^{D_{t,\perp}} = -\frac{1}{2} \frac{\partial \langle r_{\rho\phi\phi} v'' \rangle}{\partial y} - \frac{1}{2} \frac{\partial \langle r_{\rho\phi\phi} \tilde{v}'' \rangle}{\partial y}, \quad (21b)$$

$$\begin{aligned} R_{\rho\phi\phi}^{D_{t,\parallel}} &= \frac{\partial \langle r_{\rho\phi\phi} u'' \rangle}{\partial r_x} - \frac{\partial \langle r_{\rho\phi\phi} \tilde{u}'' \rangle}{\partial r_x} + \frac{\partial \langle r_{\rho\phi\phi} w'' \rangle}{\partial r_z} - \frac{\partial \langle r_{\rho\phi\phi} \tilde{w}'' \rangle}{\partial r_z} \\ &+ \frac{1}{2} \left(\left\langle \phi'' v'' \frac{\partial \tilde{\rho}\tilde{\phi}''}{\partial y} + \rho\phi'' v'' \frac{\partial \tilde{\phi}''}{\partial y} \right\rangle + \left\langle \tilde{\phi}'' \tilde{v}'' \frac{\partial \rho\phi''}{\partial y} + \tilde{\rho}\tilde{\phi}'' \tilde{v}'' \frac{\partial \phi''}{\partial y} \right\rangle \right) \\ &- \frac{1}{2} \frac{\partial \langle r_{\rho\phi\phi} v'' \rangle}{\partial y} - \frac{1}{2} \frac{\partial \langle r_{\rho\phi\phi} \tilde{v}'' \rangle}{\partial y} + \frac{1}{2} \left\langle \tilde{\rho}\tilde{\phi}'' \phi'' \frac{\partial u_k''}{\partial x_k} + \rho\phi'' \tilde{\phi}'' \frac{\partial \tilde{u}_k''}{\partial \tilde{x}_k} \right\rangle, \end{aligned} \quad (21c)$$

where $r_{\rho\phi\phi} = \frac{1}{2}(\rho + \tilde{\rho})\phi''\tilde{\phi}''$.

With Fourier transformation, the transport equation of $R_{\rho\phi\phi}$ is converted into the wave-number space,

$$\frac{\partial E_{\rho\phi\phi}}{\partial t} = E_{\rho\phi\phi}^{P_e} + E_{\rho\phi\phi}^Q + E_{\rho\phi\phi}^{pw} + E_{\rho\phi\phi}^{vw} + E_{\rho\phi\phi}^{D_{t,\perp}} + E_{\rho\phi\phi}^{D_{t,\parallel}} + E_{\rho\phi\phi}^{D_{t,x}} + E_{\rho\phi\phi}^C + E_{\rho\phi\phi}^M. \quad (22)$$

As a complement to (10), Eq. (22) implements a spectral decomposition on the transport equation of the turbulence internal energy, which will be used to examine the spectral distributions of the internal energy transport across space and scales, and among components.

III. DIRECT NUMERICAL SIMULATION OF HYPERSONIC TURBULENT BOUNDARY LAYERS

Direct numerical simulations (DNSs) of hypersonic turbulent boundary layers are performed with a finite differencing solver, STREAMS (Supersonic TuRbulEnt Accelerated navier-stokes Solver), which was developed by Bernardini *et al.* [48]. It solves the three-dimensional compressible Navier-Stokes equations for a perfect heat-conducting gas. The viscosity coefficient is calculated by Sutherland's law. The thermal conductivity coefficient K is calculated by $K = C_p \mu / \text{Pr}$, where C_p is the specific heat at constant pressure, and Pr is the molecular Prandtl number being a constant of 0.72. The specific heat ratio γ is assumed to be equal to 1.4. The convective terms are discretized with a hybrid sixth-order energy-conserving/fifth-order weighted essentially nonoscillatory (WENO) scheme [49]. The viscous terms are approximated with a sixth-order central difference scheme. For time advancing, a three-stage, third-order Runge-Kutta scheme [50] is adopted, and the Courant-Friedrichs-Lewy (CFL) number is set less than unity. Periodic boundary conditions are

TABLE I. Flow properties at the considered location and the initial and final time considered for collecting flow samples. (T_0 and T_f represent the initial and final time considered for sample collection.)

Case	M_∞	Re_τ	T_w/T_r	$\text{Re}_{\delta_{in}}$	Re_θ	Re_{δ_2}	H_{12}	$T_0 u_\infty / \delta_{in}$	$T_f u_\infty / \delta_{in}$
<i>adiabatic</i>	5.86	416	1.0	277949.3	15068	2040	14.9	156.87	549.60
<i>cold1</i>	5.86	419	0.76	175169.9	10864	1842	12.84	97.07	269.86
<i>cold2</i>	5.86	425	0.25	21167.0	2122	1074	8.19	111.41	293.69

employed in the spanwise direction. The nonreflecting boundary conditions [51] are imposed at the upper and outflow boundaries. The isothermal no-slip conditions are used at the walls. The flow is initialized with a mean field of fully developed compressible turbulent boundary layer, with velocity fluctuations superposed at the inlet boundary via a synthetic digital filtering approach [52]. More details on boundary and initial conditions can be retrieved in Bernardini *et al.* [48].

In the present study, three DNSs of spatially developing, zero-pressure-gradient hypersonic turbulent boundary layers are carried out at freestream Mach number 5.86. The wall-to-recovery temperature ratio T_w/T_r is set as 1.0, 0.76, and 0.25, which are named *adiabatic*, *cold1*, and *cold2*, respectively. The T_r is the nominal recovery temperature determined by $T_r = T_\infty[1 + r(\gamma - 1)M_\infty^2/2]$, $r = 0.89$. The inflow Reynolds number $\text{Re}_{\delta_{in}} (= \rho_\infty u_\infty \delta_{in} / \mu_\infty)$ is adjusted to make the corresponding local friction Reynolds number $\text{Re}_\tau (= \rho_w u_\tau \delta_{99} / \mu_w)$ at approximately 420, where the subscript ∞ denotes the freestream values and w denotes the variables at the wall, δ_{in} and δ_{99} are the 99% boundary-layer thickness at the inflow station and the considered location x_{target} , respectively, and u_τ is the friction velocity calculated by $\sqrt{\tau_w / \rho_w}$, with τ_w being the wall shear stress. Additional details in terms of the local Reynolds numbers $\text{Re}_\theta (= \rho_\infty u_\infty \theta / \mu_\infty)$, $\text{Re}_{\delta_2} (= \rho_\infty u_\infty \theta / \mu_w)$, and shape factor $H_{12} (= \delta^* / \theta)$ are listed in Table I, with δ^* and θ being the displacement thickness and momentum thickness, respectively. In the present research we choose to match Re_τ mainly based on the previous literature [26,34,53] and also to limit the computational costs. If we choose to match a different definition of Reynolds number, differences may occur but the qualitative trend of the variations of coherent structures with regard to the wall-cooling intensity remains unchanged; see Duan *et al.* [11] who chose Re_{δ_2} for an example. For the statistical ensemble, the flow fields are collected during a time period more than $100\delta_{in}/u_\infty$.

Table II shows the computational domain and the grid resolutions. The computational domain is set as $L_x \times L_y \times L_z = 60\delta_{in} \times 10\delta_{in} \times 3\pi\delta_{in}$, which is discretized using $N_x \times N_y \times N_z$ grid points in the x (streamwise), y (wall-normal), and z (spanwise) direction, respectively. In the streamwise and spanwise directions, the mesh is uniformly distributed, whereas in the wall-normal direction the mesh is hyperbolically stretched to cluster grid points close to the wall. In the wall-normal direction, the grid spacings at the wall and edge of the boundary layer, Δy_w^+ and Δy_δ^+ , are less than 0.5 and 7.4, respectively, and grid spacings in the streamwise and spanwise directions, Δx^+ and Δz^+ , are less than 7.1 and 5, respectively, satisfying the requirements of DNS. The superscript $+$ denotes normalization by viscous units, namely, using the wall density ρ_w , the friction velocity u_τ , and the viscous length $\delta_v = \mu_w / (\rho_w u_\tau)$.

An examination on the adequacy of the mesh is conducted. In Fig. 1 we show the spanwise spectral distributions of the density-weighted streamwise velocity fluctuations at $y^+ = 15$ and

TABLE II. Details of the computational domains and grid resolutions.

Case	$L_x \times L_y \times L_z$	$N_x \times N_y \times N_z$	Δy_w^+	Δy_δ^+	Δx^+	Δz^+	x_{target}
<i>adiabatic</i>	$60\delta_{in} \times 10\delta_{in} \times 3\pi\delta_{in}$	$3400 \times 480 \times 580$	0.45	6.03	5.10	4.69	$56.47\delta_{in}$
<i>cold1</i>	$60\delta_{in} \times 10\delta_{in} \times 3\pi\delta_{in}$	$3000 \times 360 \times 600$	0.22	7.31	5.65	4.44	$56.00\delta_{in}$
<i>cold2</i>	$60\delta_{in} \times 10\delta_{in} \times 3\pi\delta_{in}$	$2106 \times 336 \times 512$	0.27	6.86	7.10	4.39	$53.57\delta_{in}$

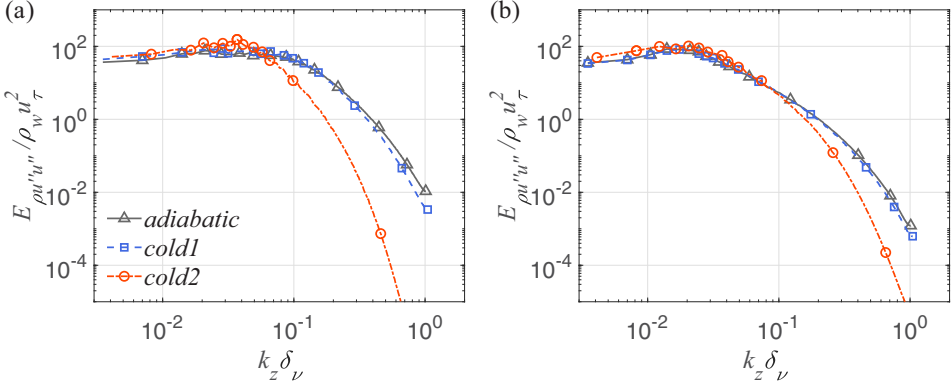


FIG. 1. Spectral distributions of density-weighted streamwise velocity fluctuations in the spanwise direction at (a) $y^+ = 15$ and (b) $y^+ = 100$.

$y^+ = 100$. The absence of energy pileup at the high-wave-number end confirms that there is no numerical energy drain in the DNSs, indicating that the spanwise grid resolution is sufficient to resolve all energetically relevant scales [13]. Furthermore, to ensure the feasibility of the synthetic digital filtering approach in hypersonic turbulent boundary layers, the distributions of wall pressure fluctuations, normalized by the local wall shear stress, are also examined as a function of friction Reynolds number. As displayed in Fig. 2, the intensities of pressure fluctuations are in good agreement with the DNS data of Huang *et al.* [54]. At last, the DNS statistical profiles of the mean streamwise velocity with van Driest transformation, $\{u\}_{vd}^+$, and the Reynolds stress, $\langle \rho u'' u'' \rangle^+$, $\langle \rho v'' v'' \rangle^+$, and $\langle \rho w'' w'' \rangle^+$ and $\langle \rho u'' v'' \rangle^+$, at $T_w/T_r = 0.76$ and 0.25 are compared with results in Zhang *et al.* [26]. As shown in Fig. 3, good agreements are found, confirming the reliability of the present DNS database.

IV. SPECTRAL ANALYSIS OF TURBULENCE KINETIC ENERGY BUDGETS

In this section we pay attention to the evolution processes of turbulence kinetic energy (TKE). The spectra of two-point velocity correlations $R_{\rho u, u_i}$ ($i = 1, 2, 3$) are first examined, followed by the discussions on the spectra of turbulence kinetic energy production, viscous dissipation, pressure strain, and turbulence kinetic energy transport. The one-dimensional spectra are only examined in

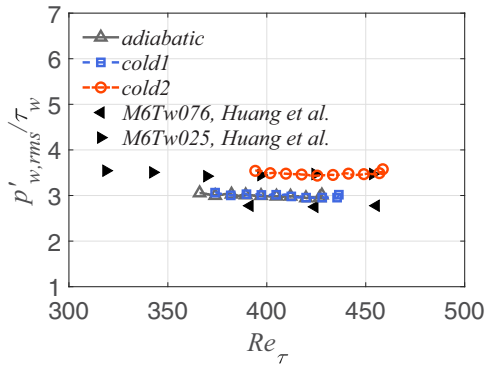


FIG. 2. Intensity of wall pressure fluctuation normalized by the local wall shear stress $p'_{w,rms}/\tau_w$ as a function of friction Reynolds number. The solid triangular symbols denote the DNS data in Huang *et al.* [54].

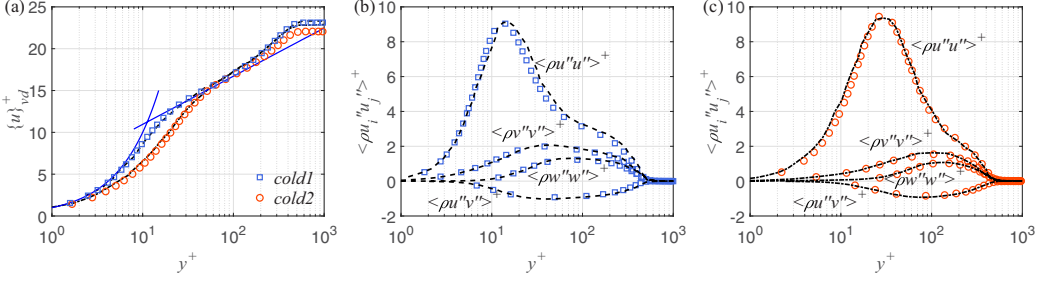


FIG. 3. Wall-normal profiles of (a) mean streamwise velocity with van Driest transformation, (b) density-weighted Reynolds stress at $T_w/T_r = 0.76$, and (c) density-weighted Reynolds stress at $T_w/T_r = 0.25$. The black dashed line and the black dot-dashed line represents the matching reference cases in Zhang *et al.* [26]. The blue solid lines in (a) denote the linear law of the wall $\{u\}^+ = y^+$ and the incompressible logarithmic law $\{u\}^+ = 2.5 \ln y^+ + 5.2$.

the spanwise direction, as the scale separation tends to be more evident in the spanwise direction at relatively low Reynolds numbers [36,55], and the energy-containing eddies can be well characterized by their spanwise wavelengths [56].

A. Turbulence kinetic energy

Figure 4 displays the wall-normal profiles of the three components of turbulence kinetic energy, $\langle \rho u'' u'' \rangle^+$, $\langle \rho v'' v'' \rangle^+$, and $\langle \rho w'' w'' \rangle^+$. The magnitudes shown in Fig. 4 suggest major contributions of turbulence kinetic energy from the main stream. In the *adiabatic* case, the inner peak of $\langle \rho u'' u'' \rangle^+$ locates at $y^+ \approx 13$. The logarithmic variations of $\langle \rho u'' u'' \rangle^+$ and $\langle \rho w'' w'' \rangle^+$, as marked by the dashed lines in panels (a) and (c), and the near-wall plateau of $\langle \rho v'' v'' \rangle^+$ are observed, consistent with the prediction of the attached eddy hypothesis [54,57].

When the wall temperature decreases, the locations of the TKE peaks are shifted away from the wall (in terms of viscous units); the peak magnitude of $\langle \rho u'' u'' \rangle^+$ is slightly increased, whereas those of $\langle \rho v'' v'' \rangle^+$ and $\langle \rho w'' w'' \rangle^+$ are decreased, which are also reported by Huang *et al.* [54]. In the *cold2* case, the strong wall cooling makes it obscure to identify the logarithmic variations of $\langle \rho u'' u'' \rangle^+$ and $\langle \rho w'' w'' \rangle^+$, and enhances $\langle \rho v'' v'' \rangle^+$ exceptionally in the very-near-wall region ($y^+ < 6$). To eliminate the wall-temperature effects and collapse the Reynolds normal stress profiles onto a unified curve, various transformations have been proposed [19,26,58]. However, the compressibility transformation to map the statistical profiles to an equivalent incompressible flow

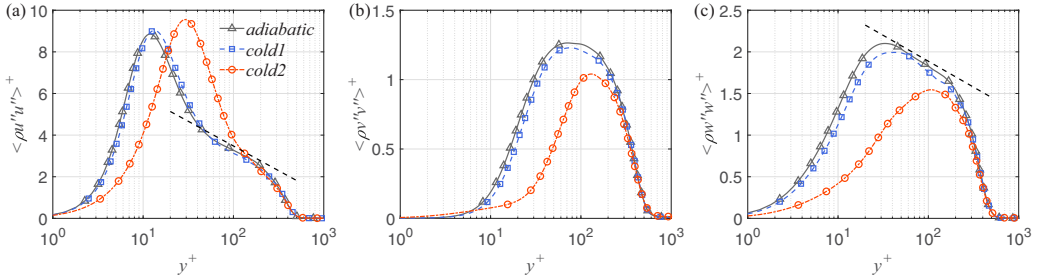


FIG. 4. Wall-normal profiles of (a) $\langle \rho u'' u'' \rangle^+$, (b) $\langle \rho v'' v'' \rangle^+$, and (c) $\langle \rho w'' w'' \rangle^+$ in the hypersonic turbulent boundary layers under three wall conditions. The black dashed line in panel (a) denotes $\langle \rho u'' u'' \rangle^+ = 8.22 - 1.03 \log y^+$ and that in (c) $\langle \rho w'' w'' \rangle^+ = 3.13 - 0.27 \log y^+$.

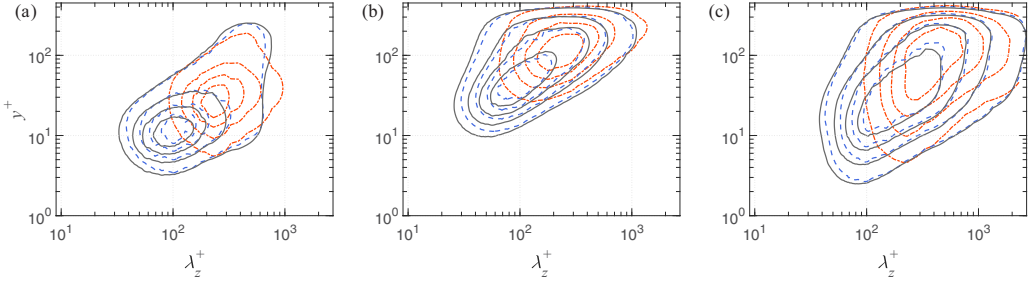


FIG. 5. Spanwise premultiplied spectra (a) $k_z E_{\rho uu}^+$, (b) $k_z E_{\rho vv}^+$, and (c) $k_z E_{\rho ww}^+$ in the hypersonic turbulent boundary layers under three wall conditions. The gray solid line, blue dashed line, and orange dot-dashed line denote the *adiabatic*, *cold1*, and *cold2* case, respectively. The contour lines indicate 0.2, 0.4, 0.6, and 0.8 of their maxima, from outside to inside; the same for the following contours if not specially stated.

by taking thermodynamics into account is out of the scope of the present study, and we will not discuss it hereafter.

Figure 5 plots the spanwise premultiplied spectra of the TKE components, $k_z E_{\rho uu}^+$, $k_z E_{\rho vv}^+$, and $k_z E_{\rho ww}^+$. In the *adiabatic* case, the streamwise energy spectra $k_z E_{\rho uu}^+$ exhibit an inner peak at $\lambda_z^+ \approx 100$, which characterizes the spanwise spacing of the near-wall coherent structures, similar to the features in incompressible wall turbulence [56,59]. A second peak appears at $(\lambda_z/\delta_{99}, y^+) \approx (1.0, 100)$, although it is not apparent at the present relatively low Reynolds number. The second peak represents the dynamics of large- and very-large-scale motions in the outer region [60–62]. The spectra $k_z E_{\rho vv}^+$ in the *adiabatic* case are more intense within $y^+ = 20 \sim 100$, since the impermeability of the wall limits the wall-normal fluctuations from extending close to the near-wall region. The spectral peaks of $k_z E_{\rho vv}^+$ and $k_z E_{\rho ww}^+$ locate at $\lambda_z^+ \approx 100$ and $\lambda_z^+ \approx 150$, respectively, which is indicative of the near-wall quasistreamwise vortical structures [56,63]. In the cold-wall cases, the weak wall cooling ($T_w/T_r = 0.76$) does not influence the spectral distributions significantly, neither in scales nor in space, but the other ($T_w/T_r = 0.25$) does. It can be seen that in the *cold2* case, the spanwise wavelengths of all TKE components are remarkably enlarged, with their peaks lifted up simultaneously. The second peak in the spectra $k_z E_{\rho uu}^+$ becomes ambiguous, indicating the reduction of separation between the viscous- and outer-scale motions [54].

More features of the energy distributions can be gained from the two-dimensional premultiplied spectra, as shown in Fig. 6. Given that the flow is assumed to be quasiperiodic in the streamwise direction, we perform two-dimensional Fourier transformation of the fluctuations, which are obtained by subtracting the local mean quantity at a streamwise location from the instantaneous signals. Three positions at $y^+ = 15, 100,$ and 200 are selected to characterize the features in the inner, logarithmic, and outer region, respectively. Note $y^+ = 200$ amounts to $y/\delta_{99} \approx 0.5$. In the inner region, the Fourier modes of $k_x k_z E_{\rho uu}^+$ are mostly concentrated in the region where $\lambda_x^+ > \lambda_z^+$, which is ascribed to the near-wall streaks elongated in the streamwise direction. In the *adiabatic* case, the spectra peak at $(\lambda_x^+, \lambda_z^+) \approx (500, 100)$. Wall cooling has an effect to enlarge the wavelengths of the local $\langle \rho u'' u'' \rangle$ structures, although only trivial deviations are found in the *cold1* case with weak wall cooling [see Fig. 6(a)]. The spectra $k_x k_z E_{\rho vv}^+$ and $k_x k_z E_{\rho ww}^+$ at $y^+ = 15$, drawn in Figs. 6(b) and 6(c), respectively, exhibit similar wall-temperature effects as those in $k_x k_z E_{\rho uu}^+$. One remarkable feature in the *cold2* case is that $k_x k_z E_{\rho vv}^+$ tends to spread significantly in the spanwise-elongated region, i.e., $\lambda_z^+ > \lambda_x^+$, indicating that the strong wall cooling renders much stronger spanwise coherence of the vertical motions than their streamwise organization.

To give further insights into the scales of turbulent structures at $y^+ = 15$, autocorrelations of u'' , v'' , and w'' ($R_{u''u''}$, $R_{v''v''}$, and $R_{w''w''}$) in the streamwise and spanwise directions are calculated and shown in Fig. 7. We can see that as the wall temperature decreases, the widths of streamwise

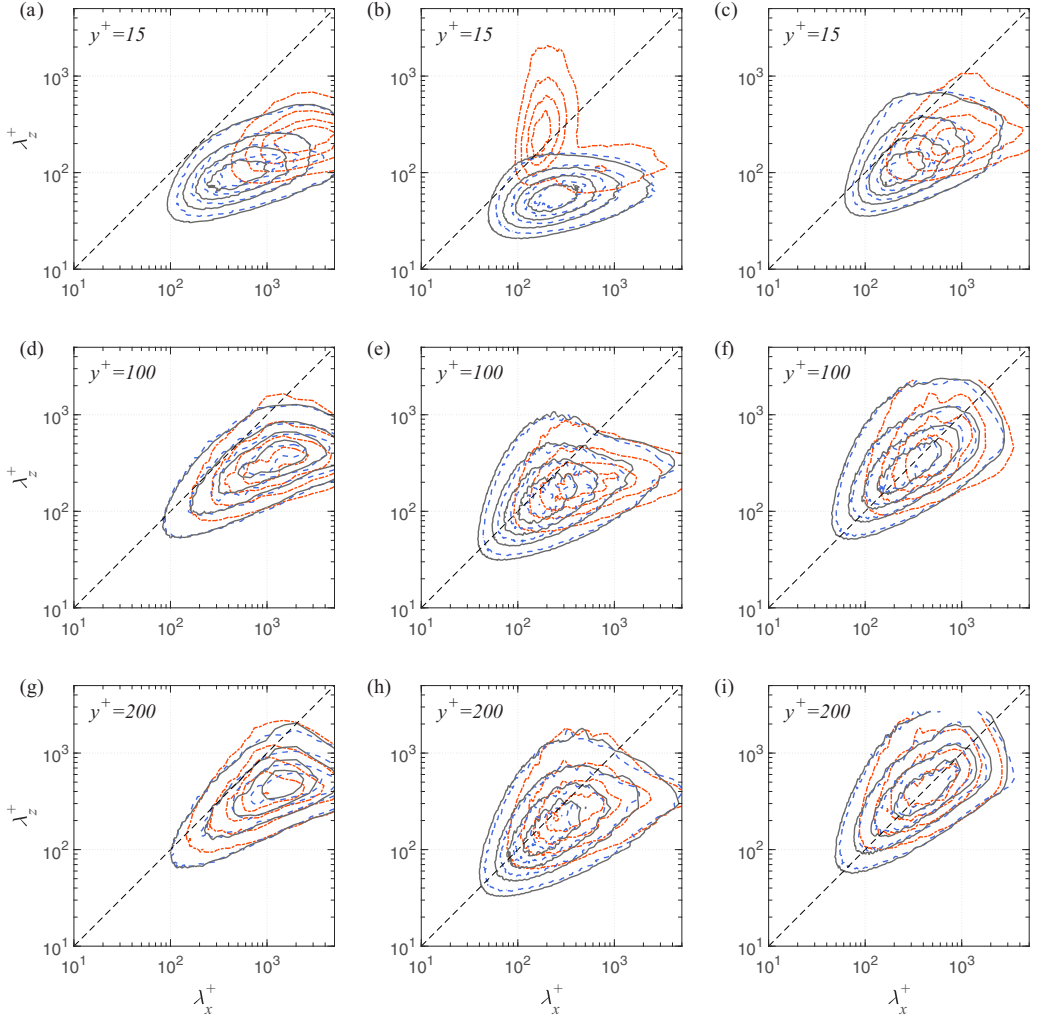


FIG. 6. Two-dimensional premultiplied spectra, (a), (d), (g) $k_x k_z E_{\rho uu}^+$, (b), (e), (h) $k_x k_z E_{\rho vv}^+$, and (c), (f), (i) $k_x k_z E_{\rho ww}^+$, at $y^+ = 15, 100,$ and $200,$ in the hypersonic turbulent boundary layers under three wall conditions. Legends refer to Fig. 5. The diagonal dashed line denotes $\lambda_x^+ = \lambda_z^+.$

autocorrelations of u'' and w'' are increased significantly in the *cold2* case, while that of $R_{v''v''}$ varies slightly, which is consistent with the phenomenon in Figs. 6(a)–6(c). In panel (d), the spanwise correlation of u'' structures at $T_w/T_r = 0.76$ almost collapses to that at $T_w/T_r = 1.0,$ whereas an obvious division is visible for the *cold2* case at $T_w/T_r = 0.25.$ For the spanwise autocorrelation of v'' [panel (e)], its spacing is apparently increased by wall cooling in comparison with the mildly influenced streamwise autocorrelation in panel (b), leading to the spanwise-oriented v'' structures plotted in Fig. 6(b). At last in panel (f) the spanwise spacings of w'' structures are very similar to those of u'' structures. With wall cooling, larger spanwise spacing is also observed in the $R_{w''w''}$ map.

Figures 6(d)–6(i) show two-dimensional spectra of the TKE components in the logarithmic ($y^+ = 100$) and outer ($y^+ = 200$) region. The $k_x k_z E_{\rho uu}^+, k_x k_z E_{\rho vv}^+,$ and $k_x k_z E_{\rho ww}^+$ peak at larger wavelengths than those at $y^+ = 15,$ and extend more towards the spanwise direction, indicating increased spanwise coherence [64], as a consequence of the combination of the classical

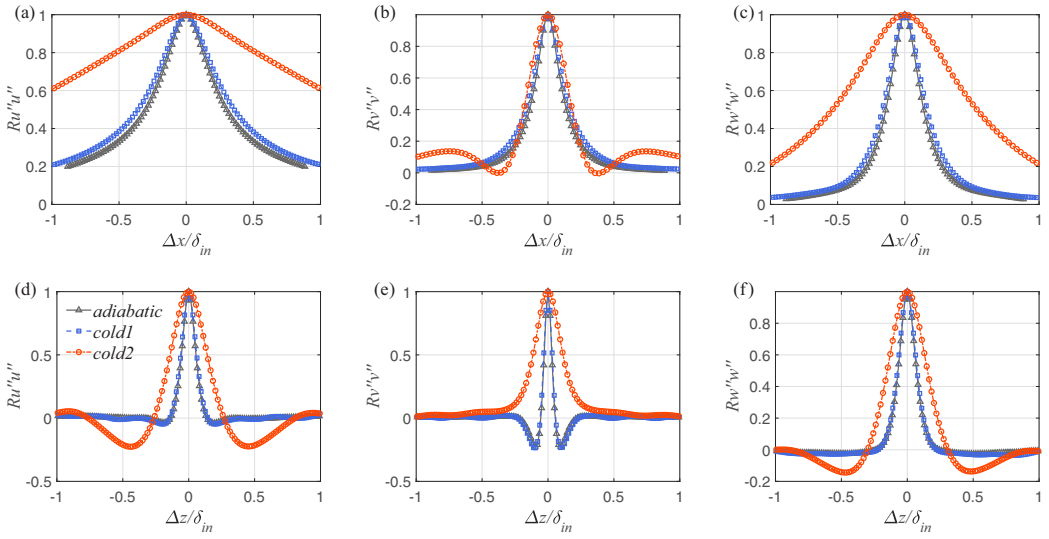


FIG. 7. Streamwise and spanwise autocorrelation of (a), (d) u'' , (b), (e), v'' , and (c), (f) w'' at $y^+ = 15$, in the hypersonic turbulent boundary layers under three wall conditions.

scale-isotropic turbulence and the streaky motions. The deviations induced by the wall temperature are, to some extent, relieved in the logarithmic and outer region. In particular, at large wavelengths the spectral distributions of three cases are quite close to each other; nonetheless, the spectra at small scales are still biased towards larger λ_x^+ and λ_z^+ with the decreasing wall temperature.

B. Turbulence kinetic energy production

The one-dimensional premultiplied spectra of the streamwise TKE production, $y^+ k_z E_{\rho u u}^{P k^+}$, are plotted in Fig. 8. The other two components in the wall-normal and spanwise directions are not shown here, as their amplitudes are too small compared with the streamwise one. Note that the one-dimensional spectra are premultiplied by y^+ and k_z to represent the energy spectral densities

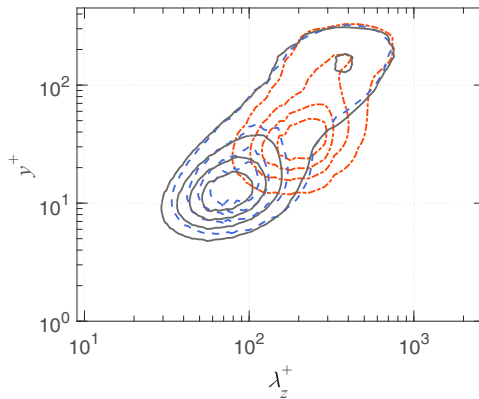


FIG. 8. Spanwise premultiplied spectra of the streamwise TKE production $y^+ k_z E_{\rho u u}^{P k^+}$ in the hypersonic turbulent boundary layers under three wall conditions. Legends refer to Fig. 5.

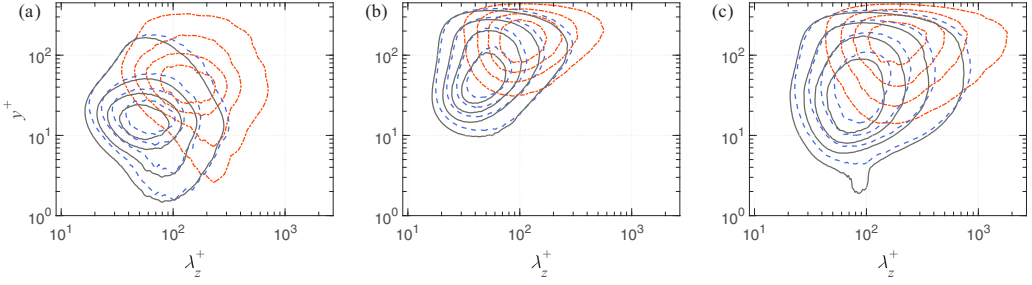


FIG. 9. Spanwise premultiplied spectra of the viscous dissipation, (a) $y^+ k_z E_{\rho uu}^{\epsilon k+}$, (b) $y^+ k_z E_{\rho vv}^{\epsilon k+}$, and (c) $y^+ k_z E_{\rho ww}^{\epsilon k+}$, in the hypersonic turbulent boundary layers under three wall conditions. Legends refer to Fig. 5.

in the logarithmic plot. As for the two-dimensional premultiplied spectra of the streamwise TKE production, they are not shown here for brevity and interested readers can refer to Appendix A 1.

In the *adiabatic* case, the distribution of $y^+ k_z E_{\rho uu}^{\epsilon k+}$ has an inner peak at $(\lambda_z^+, y^+) \approx (80, 12)$ and an outer peak at $(\lambda_z^+, y^+) \approx (385, 170)$ or $(\lambda_z/\delta_{99}, y/\delta_{99}) \approx (0.94, 0.42)$. The inner peak is linked to the near-wall streaks and quasistreamwise vortices [59], and the outer peak is associated with the self-sustaining mechanism of the outer large-scale motions [65]. The TKE production spectra are well aligned along an inclined ridge, indicating that the spanwise wavelength of the spectral peak linearly grows with the distance from the wall [66]. These features are consistent with the findings in incompressible channel flows [36].

As the wall temperature decreases, the inner peak moves upper and towards larger spanwise wavelengths, e.g., locating at $(\lambda_z^+, y^+) \approx (230, 35)$ in the *cold2* case, whereas the location of the outer peak is barely influenced. It suggests that the wall cooling has actions to suppress the production of streamwise TKE associated with the near-wall small-scale motions. The linearly distributed ridge exhibits a gradually decreasing rate of the spanwise scale with regard to the wall-normal distance, which is conspicuous in the *cold2* case.

C. Viscous dissipation

Figure 9 displays the spanwise premultiplied spectra of the viscous dissipation in three directions, i.e., $y^+ k_z E_{\rho uu}^{\epsilon k+}$, $y^+ k_z E_{\rho vv}^{\epsilon k+}$, and $y^+ k_z E_{\rho ww}^{\epsilon k+}$, in the light of Eq. (6b). In the *adiabatic* case, the spectrum $y^+ k_z E_{\rho uu}^{\epsilon k+}$ peaks at $(\lambda_z^+, y^+) \approx (56, 14)$. In general, the contribution to $y^+ k_z E_{\rho uu}^{\epsilon k+}$ is mostly concentrated within the small-wavelength region, say $\lambda_z^+ < 100$ throughout the turbulent boundary layer. The prominent role of the small-scale motions in the viscous dissipation is essentially consistent with the Kolmogorov's similarity hypothesis [67] that the viscous effects are exclusively exerted on the dissipative-scale motions, which in turn take responsibility for most of the dissipation. The power-law dependence of the spanwise wavelength of the spectral peak with regard to y^+ , observed in channel flows [36], is illegible here, possibly due to the relatively low friction Reynolds number in the present study. In Fig. 9(b), the spectral distribution of $y^+ k_z E_{\rho vv}^{\epsilon k+}$ tends to be concentrated beyond the buffer layer, with its peak at $(\lambda_z^+, y^+) \approx (46, 43)$ in the *adiabatic* case. In particular, this wall-normal dissipation is zero at the wall due to the wall impermeability and no-slip condition. As for the spectral density $y^+ k_z E_{\rho ww}^{\epsilon k+}$, it peaks at $(\lambda_z^+, y^+) \approx (81, 34)$ in the *adiabatic* case and is widely distributed and extended to the wall.

When the wall temperature decreases, the spectral distributions are shifted towards larger y^+ and λ_z^+ , for all of the three components, as a result of the lifting structures with increased coherence by wall cooling [34]. The Kolmogorov length scale (η^+), characterizing the very smallest and dissipative eddies [67], is also increased in the cold-wall cases (the results are not shown here). Different from the subtle influences on the outer distributions of the TKE production in Fig. 8, the effect of wall temperature on the spectra of viscous dissipation is still active even close to the edge

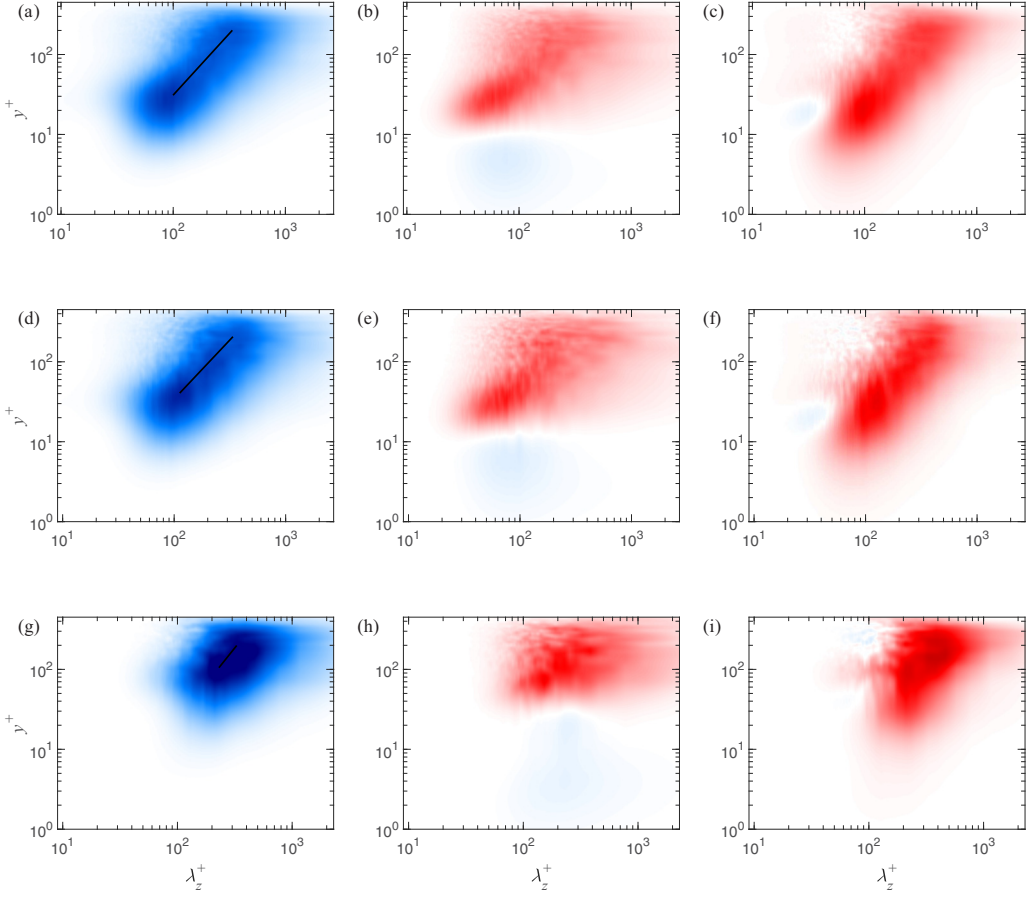


FIG. 10. Spanwise premultiplied spectra of the pressure strain, (a), (d), (g) $y^+ k_z E_{\rho u_i u_i}^{\Pi p+}$, (b), (e), (h) $y^+ k_z E_{\rho v v}^{\Pi p+}$, and (c), (f), (i) $y^+ k_z E_{\rho w w}^{\Pi p+}$, in the hypersonic turbulent boundary layers at (a)–(c) $T_w/T_r = 1.0$, (d)–(f) $T_w/T_r = 0.76$, and (g)–(i) $T_w/T_r = 0.25$. The ranges of color bar in these figures are the same, with blue to red denoting negative to positive values $[-0.8, 0.8]$.

of the boundary layer, suggesting that the small-scale motions are altered throughout the whole wall layer by the wall cooling. Consistent results can be observed in the two-dimensional premultiplied spectra of the viscous dissipation, as shown in Appendix A 2.

D. Pressure strain

Figure 10 plots the spanwise spectral densities of the pressure strain $y^+ k_z E_{\rho u_i u_i}^{\Pi p}$, which acts to redistribute the TKE among the streamwise, wall-normal, and spanwise components [36]. In Fig. 10 one of the most prominent features is the negative magnitude of $y^+ k_z E_{\rho u u}^{\Pi p+}$ and positive ones of $y^+ k_z E_{\rho v v}^{\Pi p+}$ and $y^+ k_z E_{\rho w w}^{\Pi p+}$ in most regions of the boundary layer and scale space, which indicates that the streamwise TKE is transferred to the other two components. Exceptions occur in the near-wall region of $y^+ k_z E_{\rho v v}^{\Pi p+}$ [panels (b), (e), and (h)] and the small-wavelength region of $y^+ k_z E_{\rho w w}^{\Pi p+}$ [panels (c), (f), and (i)]. Near the wall, the negative magnitude of $E_{\rho v v}^{\Pi p+}$ indicates that energy is transferred from $\langle \rho v'' v'' \rangle$ at all scales, which is expected since the presence of the impermeable wall compels the vertical velocity fluctuations to turn to the wall-parallel components. A corresponding positive $E_{\rho w w}^{\Pi p+}$ is manifest in the same region. This reveals that $\langle \rho v'' v'' \rangle$ is mainly redistributed to $\langle \rho w'' w'' \rangle$,

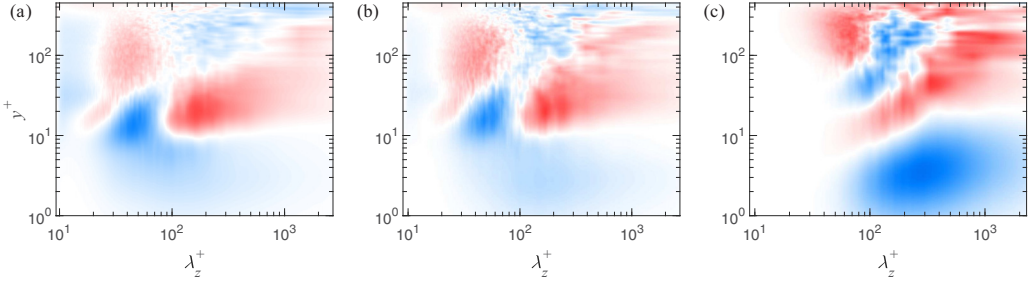


FIG. 11. Spanwise premultiplied spectra of the pressure strain $y^+ k_z \sum_{i=1}^3 E_{\rho u_i u_i}^{\Pi p+}$ in the hypersonic turbulent boundary layers at (a) $T_w/T_r = 1.0$, (b) $T_w/T_r = 0.76$, and (c) $T_w/T_r = 0.25$. The ranges of color bar in these figures are the same, with blue to red denoting negative to positive values $[-0.04, 0.04]$.

as a result of the quasistreamwise vortices [36]. On the other hand, in the spectra $y^+ k_z E_{\rho w w}^{\Pi p+}$, a weak negative region is observed at small spanwise wavelengths, for all three cases. As the corresponding spectra $E_{\rho v v}^{\Pi p+}$ at the same y^+ and λ_z^+ is observed to be positive, $\langle \rho w'' w'' \rangle$ is probably transferred towards $\langle \rho v'' v'' \rangle$. This kind of energy transfer (from the spanwise to wall-normal direction) always occurs in the streamwise-elongated ($\lambda_x^+ > \lambda_z^+$) structures (not shown) and is speculated to be associated with the streamwise vortex stretching. A comparison between $y^+ k_z E_{\rho v v}^{\Pi p+}$ and $y^+ k_z E_{\rho w w}^{\Pi p+}$ illustrates that the streamwise TKE is redistributed to the spanwise component preferentially in larger scales, whereas to the wall-normal component in smaller scales [68]. This is consistent with the phenomenon that the spanwise wavelength of w'' structures is relatively larger than that of v'' , as shown in Fig. 5. The decrease of wall-to-recovery temperature ratio will not qualitatively change the characteristics of kinetic energy redistribution, though the inner-scaled wall distance y^+ and length scale λ_z^+ of spectral peaks are increased and its intensity of energy transfer is enhanced by wall cooling [47].

At last, it is worthwhile to point out that, other than the zero trace of pressure-strain tensor in incompressible flows, $\sum_{i=1}^3 E_{\rho u_i u_i}^{\Pi p}$ is exclusively nonzero in compressible turbulence as a result of velocity dilatation. This term consequently induces interactions between the internal and kinetic energy, and it has been employed as an explicit indicator to measure the fluid genuine compressibility [5]. Figure 11 plots the spanwise premultiplied spectra of summed pressure strain, $y^+ k_z \sum_{i=1}^3 E_{\rho u_i u_i}^{\Pi p}$. It is observed that the turbulence kinetic energy is drawn and deposited into the internal component at all scales within the near-wall region, basically $y^+ < 10$. Beyond this region, two-way exchanges between the kinetic and internal energy at small and large wavelengths are mostly canceled out. Larger magnitudes of $y^+ k_z \sum_{i=1}^3 E_{\rho u_i u_i}^{\Pi p+}$ are found in the cold-wall cases, indicating that wall cooling enhances the effect of compressibility, consistent with the previous findings by Duan *et al.* [11] and Zhang *et al.* [26]. However, under the present Mach-number and wall-temperature conditions, the magnitude of summed pressure strain is still of minor significance, as the range of color bar in Fig. 11 is at least an order of magnitude smaller than that in Fig. 10. Actually, even at higher Mach numbers and lower wall-to-recovery temperature ratios, e.g., $M_\infty = 13.64$ and $T_w/T_r = 0.18$ in Zhang *et al.* [26], the contribution of pressure strain is still confined within a very-near-wall layer and is small enough to be neglected (refer to Figs. 15 and 17 in Zhang *et al.* [26]). Therefore in this paper we will not pay attention to the contribution of pressure strain to the kinetic and internal energy interactions.

E. Transport of turbulence kinetic energy among space and scales

The transport of TKE among space and scales is controlled by pressure diffusion, viscous diffusion, and turbulent convection, as seen in Eq. (17). Due to the relatively mild streamwise

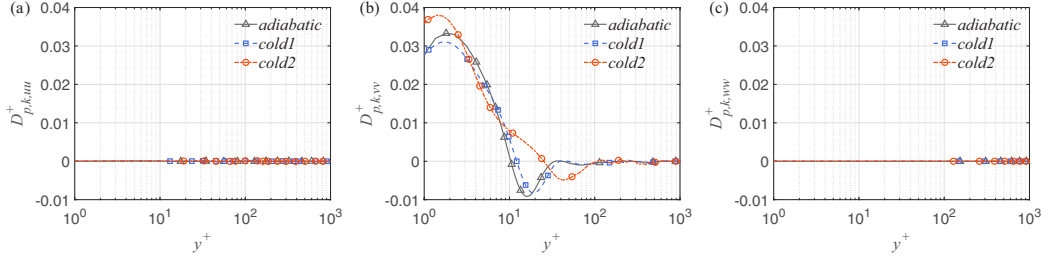


FIG. 12. Wall-normal profiles of pressure diffusion of turbulence kinetic energy, D_{p,k,u_i}^+ , in the hypersonic turbulent boundary layers under three wall conditions.

development of the boundary layer in comparison with the wall-normal statistical variations, the spatial energy transport occurs primarily in the wall-normal direction.

1. Pressure diffusion

The wall-normal profiles of pressure diffusion, $D_{p,k,u_i} = -\partial\langle p'u_i'' \rangle / \partial x_i$, are shown in Fig. 12. The streamwise and spanwise components, $D_{p,k,uu}$ and $D_{p,k,ww}$, are negligible. The wall-normal component $D_{p,k,vv}$ dominates the energy transport, from $10 < y^+ < 30$ in the *adiabatic* and *cold1* case to the near-wall region, and from $30 < y^+ < 100$ in *cold2* case. The integral of $D_{p,k,vv}$ over the wall layer is zero, corroborating the balance of pressure transport in space.

Figure 13 depicts the spanwise premultiplied spectra of pressure diffusion $y^+ k_z E_{\rho vv}^{D_{p^+}}$. The positive spectra near the wall ($y^+ < 10$) indicate energy receiving at all spanwise wavelengths, regardless of the wall temperature. Beyond the very-near-wall layer, an energy donor (negative) region is observed, with the spanwise wavelength approximately proportionally scaling with y^+ . Specifically, at large wavelengths the energy is transported from a region near the boundary-layer edge towards the near-wall region as a result of outer-layer large-scale modulation on the near-wall dynamics [60,69,70].

2. Viscous diffusion

Figure 14 shows the wall-normal profiles of viscous diffusion, $D_{v,k,u_i} = \partial\langle \tau_{ik}' u_i'' \rangle / \partial x_k$. The streamwise component takes the dominance to transport energy from a region (say, around $4 < y^+ < 15$ in the case of *adiabatic* and *cold1* and $9 < y^+ < 40$ in *cold2*), both towards the wall and away from the wall. This is also displayed in the premultiplied spectra of streamwise viscous transport $y^+ k_z E_{\rho uu}^{D_{v^+}}$ in Fig. 15. In panel (a), the positive and negative spectral peaks locate at

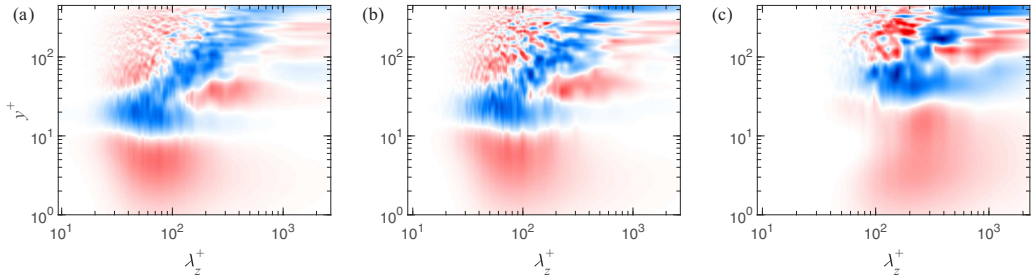


FIG. 13. Spanwise premultiplied spectra of the pressure diffusion of wall-normal TKE, $y^+ k_z E_{\rho vv}^{D_{p^+}}$, in the hypersonic turbulent boundary layers at (a) $T_w/T_r = 1.0$, (b) $T_w/T_r = 0.76$, and (c) $T_w/T_r = 0.25$. The ranges of color bar in these figures are the same, with blue to red denoting negative to positive values $[-0.2, 0.2]$.

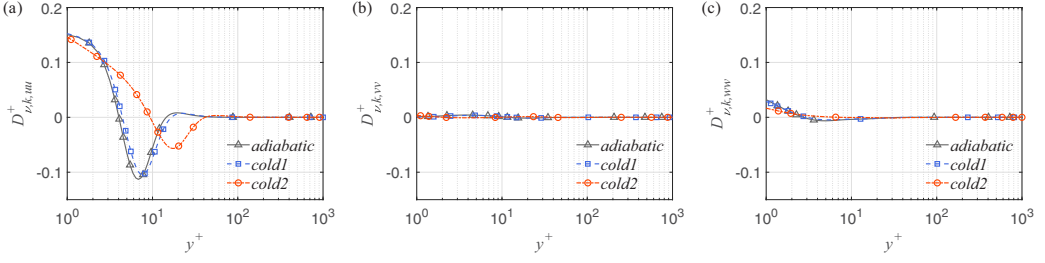


FIG. 14. Wall-normal profiles of viscous diffusion of turbulence kinetic energy, $D_{v,k,u_i u_i}^+$, in the hypersonic turbulent boundary layers under three wall conditions.

$(\lambda_z^+, y^+) \approx (80, 2.2)$ and $(80, 7.6)$, respectively, implying that the viscous transport dominantly appears at small scales in the near-wall region. From the spectra we can see that the downward/upward viscous transport exhibits in a wide range of wavelengths, with its spatial direction hinging on the wall-normal distance. Beyond the inner layer (e.g., $y > 30$ in the *adiabatic* case), there is almost no viscous diffusion at any scales. In the cold-wall cases, shown in panels (b) and (c), the peaks move to a larger λ_z^+ and a higher y^+ position. This variation is consistent with the wall-cooling effect on the characteristics of the near-wall structures, as discussed in Sec. IV B. Moreover, wall cooling acts to enhance the spectral density of viscous diffusion of TKE.

3. Turbulent convection

The turbulent convection of TKE is expressed as $D_{t,k,u_i u_i} = -1/2\partial(\rho u_i'' u_k'')/\partial x_k$, and its wall-normal profiles are shown in Fig. 16. It is found that the transport of $\langle \rho u'' u'' \rangle$ takes the dominance in the turbulent convection, and the other two components are negligibly small. As a result we only plot the turbulent-convection spectra of $\langle \rho u'' u'' \rangle$ in Fig. 17.

Since $\int_0^\infty R_{\rho u u}^{D_{t,\perp}} dy = 0$ for any r_z , the turbulent energy transfer in the y direction is examined at different spanwise wavelengths. At small λ_z^+ , $D_{t,k,\rho u u}$ transports energy both towards the wall and away from the wall, from a region corresponding to the characteristic inner-layer structures. In the large-scale region, e.g., $\lambda_z^+ > 200$ for the *adiabatic* case, the inner layer receives energy from a region extending far away from the wall, as a token of the outer-layer large-scale modulation [60,69,70]. Similar phenomenon is observed in panels (b) and (c), except that the spectra are indeed amplified, denoting the enhanced turbulent energy transfer across space by wall cooling.

On the other hand, the spanwise premultiplied spectra of the interscale TKE transport, $y^+ k_z E_{\rho u u}^{D_{t,\parallel}^+}$, $y^+ k_z E_{\rho v v}^{D_{t,\parallel}^+}$, and $y^+ k_z E_{\rho w w}^{D_{t,\parallel}^+}$, are shown in Fig. 18. Positive and negative magnitudes

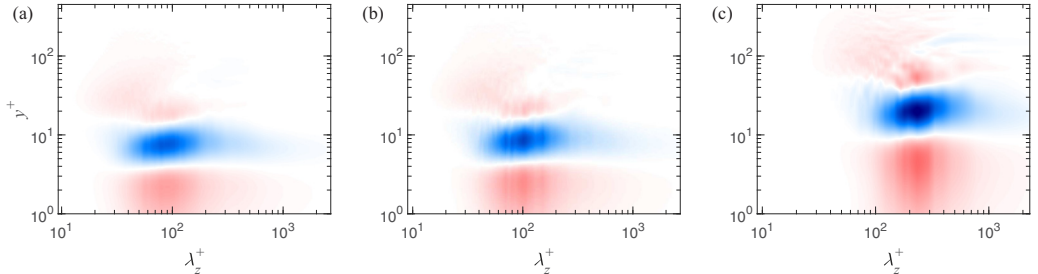


FIG. 15. Spanwise premultiplied spectra of the viscous diffusion of streamwise TKE, $y^+ k_z E_{\rho u u}^{D_{v,\parallel}^+}$, in the hypersonic turbulent boundary layers at (a) $T_w/T_r = 1.0$, (b) $T_w/T_r = 0.76$, and (c) $T_w/T_r = 0.25$. The ranges of color bar in these figures are the same, with blue to red denoting negative to positive values $[-0.8, 0.8]$.

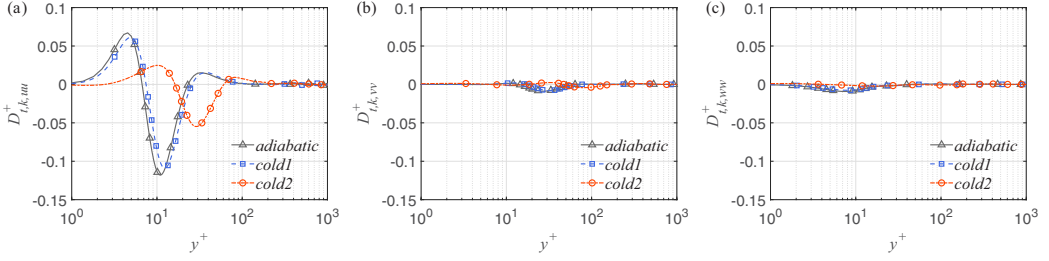


FIG. 16. Wall-normal profiles of turbulent convection of turbulence kinetic energy, $D_{t,k,uu}^+$, in the hypersonic turbulent boundary layers under three wall conditions.

in the spectra denote the energy receipt and donor in the transport process, respectively. The inclined donor regions in Figs. 18(a), 18(d) and 18(g) are aligned with the spectral distribution of TKE production in Fig. 8, and those in Figs. 18(b), 18(c), 18(e), 18(f), 18(h), and 18(i) with the wall-normal and spanwise pressure-strain spectra in Fig. 10. The receipt regions at smaller wavelengths tend to be correlated with the viscous-dissipation spectra (see Fig. 9). This reveals that the interscale turbulent convection of TKE underlies the energy exchange among components in terms of TKE budget.

Moreover, since the interscale turbulent transfer inherits the property of $\int E_{\rho u_i u_i}^{D_{t,\parallel}} dk_z = \lim_{r_z \rightarrow 0} R_{\rho u_i u_i}^{D_{t,\parallel}} = 0$ at any y , we can examine it at all specific wall distances. In Figs. 18(a), 18(d) and 18(g), the streamwise TKE ($\langle \rho u'' u'' \rangle$) is found to be transported from a region (corresponding to TKE production) to both smaller (dominant) and larger scales. The former is consistent with the energy cascade from large to small scales [67] and is particularly related to the self-sustaining mechanism, where the streaks break down and produce smaller-scale structures [71], while the latter denotes an inverse transfer, causing the large-scale structures affected by the small scales, which was also discovered by Kawata and Alfredsson [72] in the transport of Reynolds shear stress. They reported that such an inverse interscale transport acts to support the turbulent energy production at large scales away from the wall. Similar phenomenon is found in the interscale transport of spanwise TKE [see Figs. 18(c), 18(f) and 18(i)], whereas in the spectra $y^+ k_z E_{\rho v v}^{D_{t,\parallel}}$, energy is transported only from large- to small-scale motions [see Figs. 18(b), 18(e) and 18(h)]. As for the effects of wall cooling on the interscale energy transport, it is exactly the same as what we discussed above and thus will not be reiterated here.

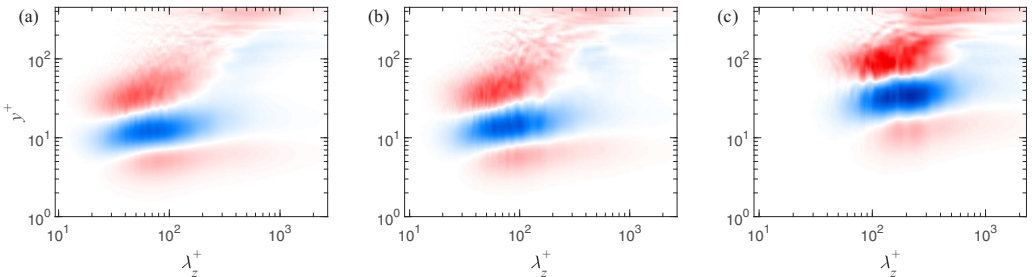


FIG. 17. Spanwise premultiplied spectra of the turbulent convection of streamwise TKE along space, $y^+ k_z E_{\rho u u}^{D_{t,\perp}}$, in the hypersonic turbulent boundary layers at (a) $T_w/T_r = 1.0$, (b) $T_w/T_r = 0.76$, and (c) $T_w/T_r = 0.25$. The ranges of color bar in these figures are the same, with blue to red denoting negative to positive values $[-1.2, 1.2]$.

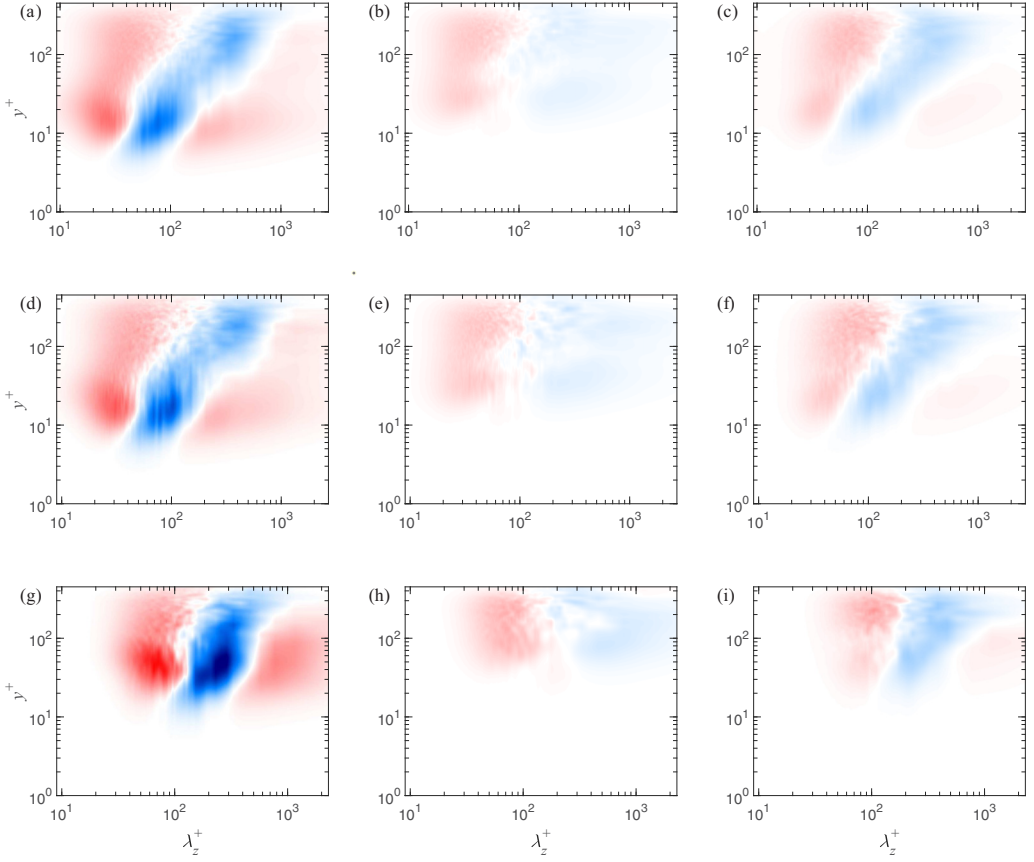


FIG. 18. Spanwise premultiplied spectra of the turbulent convection of TKE among scales, (a), (d), (g) $y^+ k_z E_{\rho u u}^{D_{r,||}^+}$, (b), (e), (h) $y^+ k_z E_{\rho v v}^{D_{r,||}^+}$, and (c), (f), (i) $y^+ k_z E_{\rho w w}^{D_{r,||}^+}$, in the hypersonic turbulent boundary layers at (a)–(c) $T_w/T_r = 1.0$, (d)–(f) $T_w/T_r = 0.76$, and (g)–(i) $T_w/T_r = 0.25$. The ranges of color bar in these figures are the same, with blue to red denoting negative to positive values $[-1.5, 1.5]$.

V. SPECTRAL ANALYSIS OF TURBULENCE INTERNAL ENERGY BUDGETS

We focus on the evolution processes of turbulence internal energy (TIE) in this section. The spectral distributions of two-point ϕ'' correlation $R_{\rho\phi\phi}$ and critical budget terms, including the turbulence internal energy production, heat conduction, and turbulence internal energy transport, are investigated.

A. Turbulence internal energy

Figure 19 shows the wall-normal profiles of turbulence internal energy, $e_t^+ = \langle \rho \phi'' \phi'' \rangle^+$, which is found to be mainly distributed in the logarithmic and outer region. Two peaks are observed at $y^+ \approx 25$ and 250, with the latter exceeding the former, in the *adiabatic* and *cold1* case. In the *cold2* case, the e_t^+ is slightly increased in $y^+ < 5$ but is greatly suppressed beyond this region. This indicates that the strong wall cooling tends to reduce the generation of TIE across the wall layer, except in the viscous sublayer.

Figure 20 plots the spanwise premultiplied spectra of TIE, $k_z E_{\rho\phi\phi}^+$. In the *adiabatic* case, two spectral peaks are observed, with the primary one located in the outer region at $(\lambda_z^+/\delta_{99}, y/\delta_{99}) \approx (1.3, 0.55)$ and the second one at $(\lambda_z^+, y^+) \approx (130, 20)$. This is essentially different from the

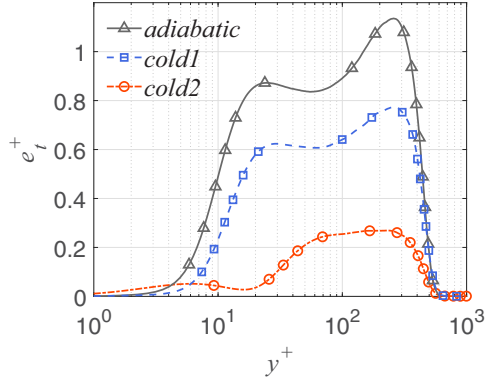


FIG. 19. Wall-normal profiles of turbulence internal energy e_t^+ in the hypersonic turbulent boundary layers under three wall conditions.

distribution of TKE, which is mainly concentrated in the inner region, at least at the present Reynolds numbers. The weak wall cooling in the *cold1* case has mild impacts on the spectral distributions, whereas in the *cold2* case the inner peak is invisible, and the outer spectra associated with the large-scale motions are barely changed.

The two-dimensional premultiplied spectra of TIE, $k_x k_z E_{\rho\phi\phi}^+$, are displayed in Fig. 21 at the three selected wall-normal distances, $y^+ = 15, 100,$ and 200 . In panel (a) at $y^+ = 15$ the Fourier modes are largely concentrated within the streamwise-elongated region for the *adiabatic* and *cold1* case, which is associated with the temperature streaks in the inner region [13]. With strong wall cooling, at $T_w/T_r = 0.25$, the spanwise wavelength is observably enlarged, with energy peaks roughly along the diagonal ($\lambda_x^+ = \lambda_z^+$).

To check the effects of wall temperature on the coherence of the ϕ'' structure at $y^+ = 15$, two-point autocorrelation maps are quantified in Fig. 22. We can see that weak wall cooling in the *cold1* case has less impact on the coherence, but the strong wall cooling in the *cold2* case enlarges the coherence both in the streamwise and spanwise direction.

In the logarithmic ($y^+ = 100$) and outer ($y^+ = 200$) region, shown in Figs. 21(b) and 21(c), large amounts of TIE are carried by the larger-scale motions, which exhibit a tendency to scale isotropy away from the wall. The effects of wall cooling on the ϕ'' structure are apparent at small wavelengths

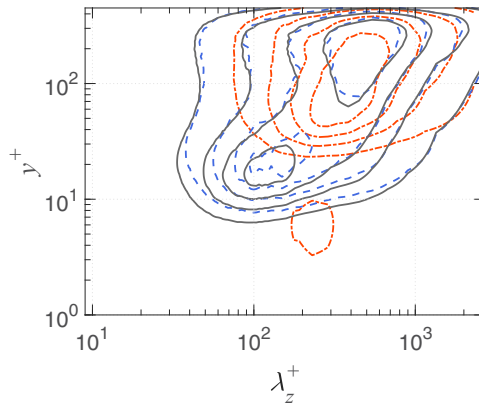


FIG. 20. Spanwise premultiplied spectra $k_z E_{\rho\phi\phi}^+$ in the hypersonic turbulent boundary layers under three wall conditions. Legends refer to Fig. 5.

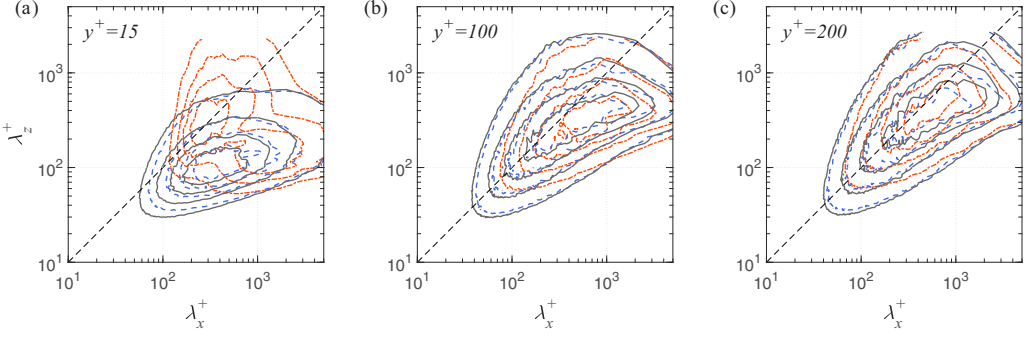


FIG. 21. Two-dimensional premultiplied spectra $k_x k_z E_{\rho\phi\phi}^+$, at (a) $y^+ = 15$, (b) $y^+ = 100$, and (c) $y^+ = 200$, in the hypersonic turbulent boundary layers under three wall conditions. Legends refer to Fig. 5.

but trivial at large scales, similar to the observations from the spectral distributions of TKE in Fig. 6. This suggests that the wall temperature has similar impacts on the structure sizes of the dynamical variables (u'' , v'' , w'') and the thermodynamical variable (ϕ'') across the wall layer.

B. Turbulence internal energy production

On the basis of Eq. (18a), Fig. 23 plots the spanwise premultiplied spectra of the TIE production, $y^+ k_z E_{\rho\phi\phi}^{P_e+}$. Prominent contributions of the TIE production are visualized particularly in the outer region, which is consistent with the observations in Figs. 19 and 20. In the *adiabatic* case, the spectral distribution has two peaks. The primary one is dominated by the large-scale motions in the outer region at $(\lambda_z^+, y^+) \approx (385, 200)$ or $(\lambda_z/\delta_{99}, y/\delta_{99}) \approx (0.93, 0.48)$, and the second one locates at $(\lambda_z^+, y^+) \approx (80, 16)$, which is related to the small-scale thermodynamic structures in the inner layer. The two peaks are connected with an inclined ridge, indicating the self-similar nature of wall-normal heat flux ($\langle \rho\phi''v'' \rangle$) from $y^+ = 16$ to 200, which is inherently reminiscent of the characteristics of Reynolds shear stress.

The influences of wall cooling on the internal-energy-containing motions are found to be similar to those we discussed in Sec. IV B. With the strong wall cooling (*cold2* case), the spectral peak in the inner region is barely visible, and most of the TIE is produced in the outer region. The turbulent dynamics beyond $y^+ \leq 50$ account for more than 75% of the total amount of TIE production.

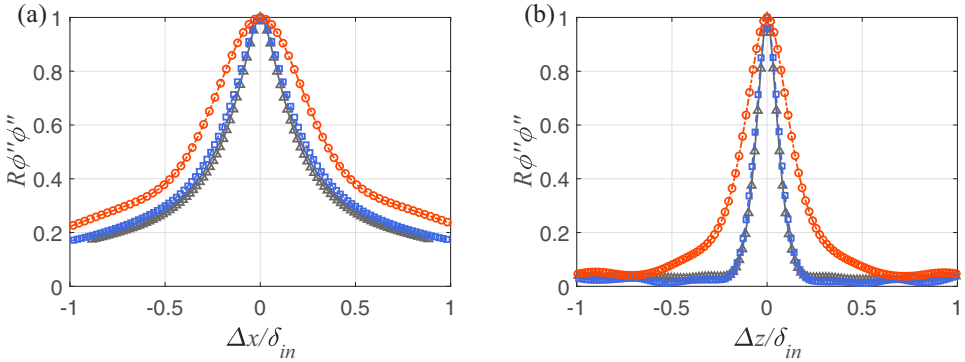


FIG. 22. Streamwise and spanwise autocorrelation of ϕ'' at $y^+ = 15$ in the hypersonic turbulent boundary layers under three wall conditions. Legends refer to Fig. 7(d).

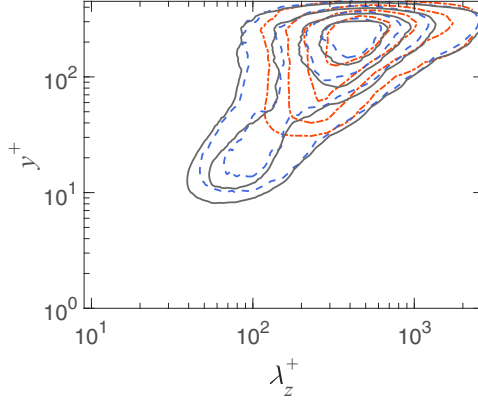


FIG. 23. Spanwise premultiplied spectra of the TIE production $y^+ k_z E_{\rho\phi\phi}^{Pe+}$, in the hypersonic turbulent boundary layers under three wall conditions. Legends refer to Fig. 5.

This confirms the reduction of scale separation under wall cooling [54]. Additional information is provided by the two-dimensional premultiplied spectra, which is discussed in Appendix A 3.

C. Heat conduction

The action of heat conduction is of particular importance in compressible turbulent boundary layers, which plays a significant role in the evolution of TIE. Figure 24 plots its one-dimensional spanwise premultiplied spectra $y^+ k_z E_{\rho\phi\phi}^{Q+}$ (with its two-dimensional premultiplied spectra given in Appendix A 4). The Fourier modes are mostly concentrated within the small scales in the outer region, and the spectral peak locates at $(\lambda_z^+, y^+) \approx (42, 200)$, $(50, 200)$, and $(100, 240)$ in the *adiabatic*, *cold1*, and *cold2* case, respectively. This suggests that the thermal energy is mostly carried and transferred by the small-scale motions throughout the boundary layer. Note that the spectral density $y^+ k_z E_{\rho\phi\phi}^Q$ is always negative, yielding energy transfer from the fluctuating to the mean field [47]. The source is probably the interscale transfer from the dominant TIE production at larger scales, which will be discussed in the next section.

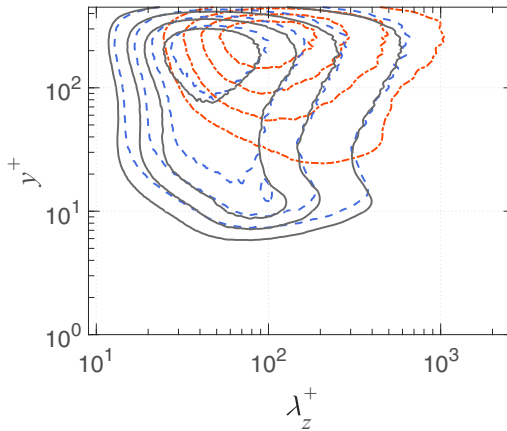


FIG. 24. Spanwise premultiplied spectra of the contribution by heat conduction $y^+ k_z E_{\rho\phi\phi}^{Q+}$, in the hypersonic turbulent boundary layers under three wall conditions. Legends refer to Fig. 5.

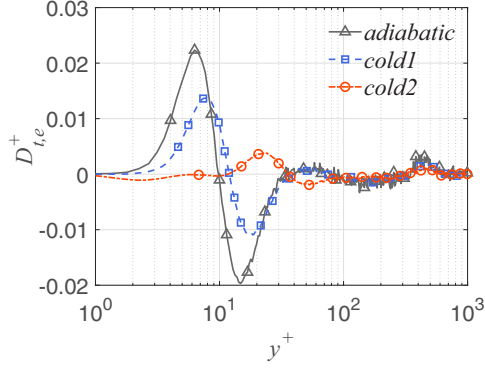


FIG. 25. Wall-normal profiles of turbulent convection of TIE, $D_{t,e}^+$, in the hypersonic turbulent boundary layers under three wall conditions.

D. Turbulent convection of turbulence internal energy among space and scales

The turbulent convection term, $D_{t,e} = -\partial\langle\rho\phi''\phi''u_k''\rangle/\partial x_k$, redistributes the TIE among space and scales to locally balance the energy gain and loss as a result of the dynamics of turbulent motions. Its wall-normal profile is plotted in Fig. 25. In the *adiabatic* case, the transport of $\langle\rho\phi''\phi''\rangle$ is mainly convected from the region $y^+ = 10 \sim 30$ to the near-wall region ($y^+ < 10$). When the wall is cooled, this type of transport tends to be attenuated and shifted away from the wall in terms of y^+ .

As suggested by Eqs. (21a)–(21c), the TIE convection can be further decomposed into energy transport associated with the streamwise heterogeneity, along the y direction and across scales. The contribution of streamwise heterogeneity is not reported here, as its magnitude is affirmed to be ignorable in the present cases under scrutiny.

Figure 26 shows the spanwise premultiplied spectra $y^+k_z E_{\rho\phi\phi}^{D_{t,\perp}^+}$. In the small-wavelength region ($\lambda_z^+ < 200$), $D_{t,e}$ transports internal energy both towards the wall and away from the wall, from a region centering around $(\lambda_z^+, y^+) \approx (86, 15)$, which corresponds well with the second peak of TIE production spectra (see Fig. 23), and is closely related to the characteristic near-wall structures. At large wavelengths the internal energy is deposited near the wall from regions far from the wall. Decreasing the wall temperature does not qualitatively change the features of TIE turbulent convection but makes the spectral distribution clustered at larger λ_z^+ and y^+ , since the near-wall structures are enlarged and lifted up in the viscous units.

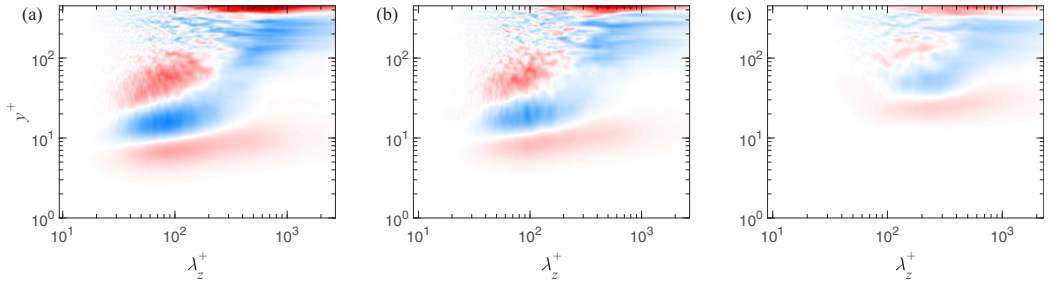


FIG. 26. Spanwise premultiplied spectra of the turbulent convection of TIE among space, $y^+k_z E_{\rho\phi\phi}^{D_{t,\perp}^+}$, in the hypersonic turbulent boundary layers at (a) $T_w/T_r = 1.0$, (b) $T_w/T_r = 0.76$, and (c) $T_w/T_r = 0.25$. The ranges of color bar in these figures are the same, with blue to red denoting negative to positive values $[-0.2, 0.2]$.

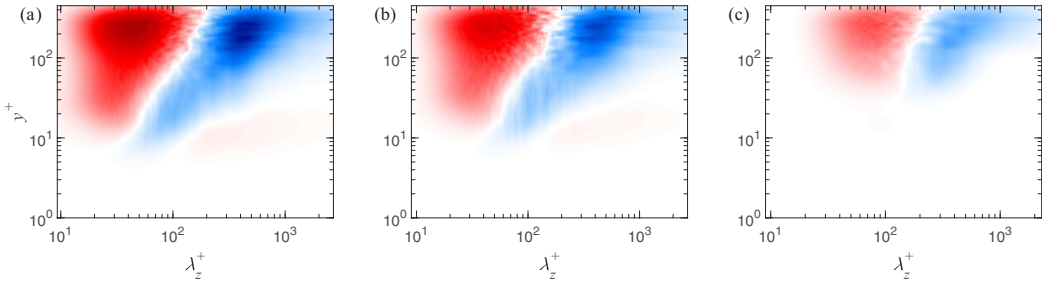


FIG. 27. Spanwise premultiplied spectra of the turbulent convection of TIE among scales, $y^+k_z E_{\rho\phi\phi}^{D_{r,\parallel}+}$, in the hypersonic turbulent boundary layers at (a) $T_w/T_r = 1.0$, (b) $T_w/T_r = 0.76$, and (c) $T_w/T_r = 0.25$. The ranges of color bar in these figures are the same, with blue to red denoting negative to positive values $[-0.5, 0.5]$.

As for the interscale TIE transport, its spanwise premultiplied spectra $y^+k_z E_{\rho\phi\phi}^{D_{r,\parallel}+}$ are shown in Fig. 27. In contrast with $y^+k_z E_{\rho\phi\phi}^{D_{r,\perp}+}$ in Fig. 26, the interscale transport takes more significant responsibility in the total TIE convection. In Fig. 27, the negative region, denoted as an energy donor, is corresponding with the spectra of TIE production as shown in Fig. 23. The positive regions represent energy recipients, which tend to be correlated with the internal energy exchange by the action of heat conduction (see Fig. 24), drawing the internal energy from the fluctuating to the mean flow field. Such alignment of the donor and recipient regions with the spectral distributions of production and heat-conduction action suggests that the interscale transport acts to promote the energy redistribution among components involved in the internal energy budget equation. Furthermore, for all of the three cases, energy was found to be primarily transported from large scales to small scales, which is consistent with the energy cascade. Near the wall, an inverse transfer from small to large scales is also observed in Figs. 27(a) and 27(b), while it is almost indiscernible with strong wall cooling in panel 27(c). At last, to obtain more comprehensive insights of interscale transport, its two-dimensional spectra are examined at $y^+ = 15$ and 100. Details are given in Appendix A 5.

VI. CONCLUSIONS

In the present study the spectral budget equations of turbulence kinetic and internal energy (TKE and TIE) are derived based on the two-point correlations of velocity and a sound-speed-like variable (ϕ), respectively. By introducing ϕ , the formulation of the TIE transport shares fully structural similarity with the TKE transport equation [47]. It allows us to investigate the spectral distributions of the budgets in the TKE and TIE transport equations in a similar manner and reveal the scale dependence of energy flow across space and scales, and among components. The spectral densities of TKE and TIE budgets, including production, dissipation, pressure strain, heat-conduction action, spatial and inter-scale transfer, are comprehensively quantified in the hypersonic turbulent boundary layers with/without wall cooling.

In the adiabatic turbulent boundary layers, the evolution processes of TKE and TIE are found to be similar, in a general sense. Nonetheless, the TKE is primarily carried by the inner-layer streamwise-elongated motions, while the TIE is mostly carried by the outer-layer nearly scale-isotropic structures, at the Reynolds number under scrutiny. The spectral density of TKE and TIE production exhibits two peaks which are well aligned along an inclined ridge, supporting the attached eddy hypothesis in terms of both dynamical and thermal structures. Differently, the inner peak, associated with the near-wall streaky and quasi-streamwise vortical motions, dominates the production of TKE, while the production of TIE is largely contributed by the large-scale modes in the outer region. The TKE production occurs mostly in the streamwise direction and will be

redistributed to the spanwise and wall-normal components via the so-called pressure strain, with the former preferentially in larger scales. However, as for the viscous dissipation of TKE and the heat conduction, which transfers the TIE from the fluctuating field to the mean-flow field, they occur at small scales across the whole wall layer, with the spanwise wavelength λ_z^+ mostly concentrated within 100. For this to happen, the TKE components and TIE are redistributed in orientation by the interscale turbulent transport, where a predominant transfer is found from the characteristic modes to smaller scales. The wall-normal interaction and modulation between the near-wall and outer-layer motions is manipulated by pressure diffusion, viscous diffusion, and turbulent transport. Notably, in compressible turbulence, the exchange between TKE and TIE is ascribed to the velocity dilatation. In the near-wall region, TKE is transferred to TIE at all wavelengths, and beyond that a two-way exchange is observed at different scales, yielding a counterbalanced energy interaction.

With wall cooling the near-wall structures are lifted up with increased coherence in terms of wall units, and the separation between the viscous- and outer-scale motions is reduced at a matching friction Reynolds number. Remarkably, strong wall cooling is able to enhance the spanwise coherence of vertical motions (v'') and thermal structures (ϕ'') greatly, in comparison with their streamwise elongation. It causes a large contribution of the spanwise-oriented modes to the wall-normal TKE and TIE in the near-wall region (at $y^+ \approx 15$). The wall cooling exerts opposite effects on the (spatial and interscale) transport of TKE and TIE, where the magnitude of the former is increased by wall cooling whereas that of the latter is suppressed. In general, we find that the effects of wall temperature exist throughout the boundary layer primarily by means of modifying the small-scale motions, and the wall cooling will not qualitatively impact the underlying mechanisms of energy evolution.

ACKNOWLEDGMENT

Funding support from the National Natural Science Foundation of China (under Grants No. 92052101 and No. 91952302) is acknowledged.

APPENDIX: TWO-DIMENSIONAL PREMULIPLIED SPECTRA OF TKE AND TIE BUDGETS

1. Turbulence kinetic energy production

Figure 28 shows the two-dimensional premultiplied spectra of the streamwise TKE production ($k_x k_z E_{\rho uu}^{Pk^+}$) at $y^+ = 15, 100,$ and 200 . Note that in order to bring out the weak spectra in the region $\lambda_z^+ > \lambda_x^+$, the contour lines in Fig. 28 denote 0.05, 0.3, 0.55, and 0.8 of their maximum. The general

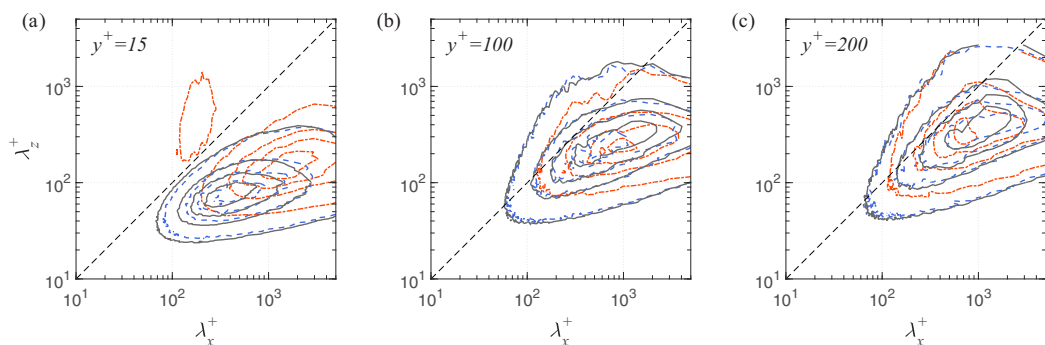


FIG. 28. Two-dimensional premultiplied spectra of the streamwise TKE production $k_x k_z E_{\rho uu}^{Pk^+}$ at (a) $y^+ = 15$, (b) $y^+ = 100$, and (c) $y^+ = 200$, in the hypersonic turbulent boundary layers under three wall conditions. Legends refer to Fig. 5, with the contour lines exceptionally denoting 0.05, 0.3, 0.55, and 0.8 of their maximum, respectively, from outside to inside.

features of the spectral distribution are very similar to those of $k_x k_z E_{\rho uu}^+$ in Fig. 6. At $y^+ = 15$, shown in Fig. 28(a), the spectra are mostly oriented in the streamwise direction, since the TKE production here is closely related to the near-wall streaks and quasistreamwise vortices. With wall cooling, the TKE tends to be generated by turbulent structures at larger streamwise and spanwise wavelengths. In particular, in the *cold2* case, a weak spectral peak appears around $\lambda_x^+ = 200$, featuring a spanwise-oriented ($\lambda_z^+ > \lambda_x^+$) energy distribution. This is related to the stronger spanwise coherence of the velocity fluctuations, especially in the wall-normal direction as depicted in Fig. 6(b).

In the logarithmic and outer regions, shown in Figs. 28(b) and 28(c), respectively, the streamwise TKE production is locally produced by large-scale motions with the increasing distance from the wall, which agrees with the observation in Fig. 8. When the wall temperature decreases, the spectra at small scales shift towards larger streamwise and spanwise wavelengths, similar to the observations in the inner region in Fig. 28(a). The spectral distributions at large scales are mildly affected by wall cooling.

2. Viscous dissipation

The two-dimensional premultiplied spectra of viscous dissipation, $k_x k_z E_{\rho uu}^{\varepsilon k^+}$, $k_x k_z E_{\rho vv}^{\varepsilon k^+}$, and $k_x k_z E_{\rho ww}^{\varepsilon k^+}$, are plotted in Fig. 29, at $y^+ = 15, 100$, and 200. In the inner region, see Figs. 29(a)–29(c), the spectra are concentrated within the region where $\lambda_x^+ > \lambda_z^+$, indicating the streamwise elongation of the energy density distributions, which is associated with the near-wall structures, such as the streaks and the quasistreamwise vortical structures. The wall cooling causes remarkable effects on the spatial elongation or spacing of dissipative motions. A striking phenomenon in the spectra $k_x k_z E_{\rho vv}^{\varepsilon k^+}$ is that the distributions, centering around $\lambda_x^+ = 100$, spread significantly towards the spanwise-oriented region where $\lambda_z^+ > \lambda_x^+$ in the *cold2* case. It is similar to the observation in the spectra $k_x k_z E_{\rho vv}^+$, shown in Fig. 6(b).

In the logarithmic and outer regions, as shown in Figs. 29(d)–29(i), the dissipation spectra $k_x k_z E_{\rho vv}^{\varepsilon k^+}$ become more isotropic among scales, whereas $k_x k_z E_{\rho uu}^{\varepsilon k^+}$ are preferentially located in $\lambda_x^+ > \lambda_z^+$ and $k_x k_z E_{\rho ww}^{\varepsilon k^+}$ in $\lambda_z^+ > \lambda_x^+$, which is consistent with the feature of isotropic turbulence [36] that the variance of the longitudinal derivatives is half that of the transverse derivatives. At last, the decrease of wall temperature increases both the streamwise and spanwise wavelengths of dissipative motions.

3. Turbulence internal energy production

In the two-dimensional premultiplied spectra $k_x k_z E_{\rho \phi \phi}^{P_e^+}$ at $y^+ = 15$, shown in Fig. 30(a), the TIE production in the inner region is primarily associated with the temperature streaks, thus yielding the streamwise-elongated feature, especially at $T_w/T_r = 1$ and 0.76. In the *cold2* case, a weak negative region appears around $(\lambda_x^+, \lambda_z^+) \approx (370, 120)$ [marked by “+” in panel (a)], which is due to the locally positive correlation of v'' and ϕ'' at the specific wave-number region. The magnitude of the negative peak is approximately -33% of the positive maximal value. The negative spectra balance with the positive ones, thus reducing the inner-layer contribution to TIE production. Note that the local negative TIE production is also observed in the other two cases but only at a limited range of wavelengths, and the peak magnitude is merely $-2\% \sim -3\%$ of the positive maximum.

Away from the wall (at $y^+ = 100$ and 200), shown in Figs. 30(b) and 30(c), the TIE production is more concentrated at larger wavelengths, which is consistent with the phenomenon in one-dimensional spanwise spectra that large-scale motions dominate the contribution to the TIE production in the outer region. At half boundary-layer thickness ($y^+ = 200$), the spectra become nearly diagonally symmetrical with respect to $\lambda_x^+ = \lambda_z^+$, which indicates that the thermodynamic structures related to the TIE production are approximately isotropically distributed in scales.

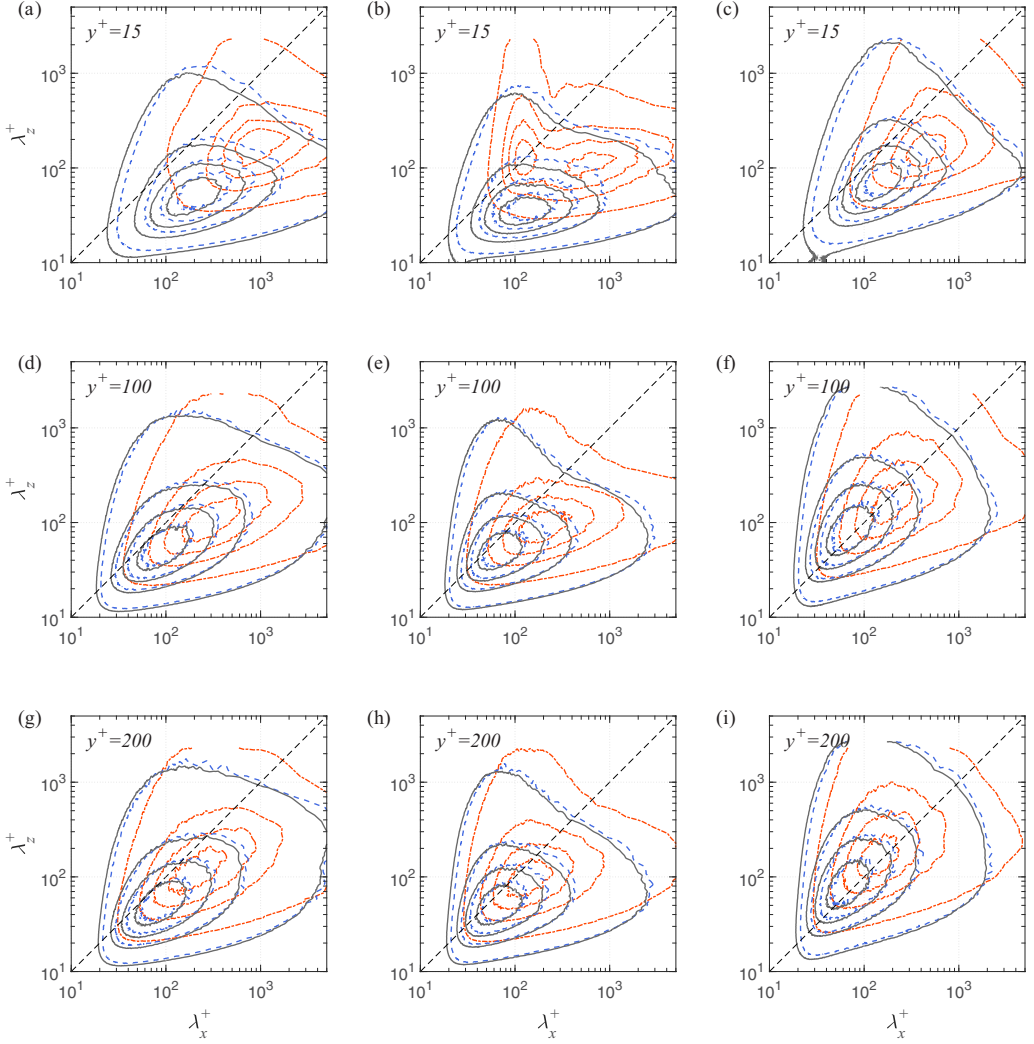


FIG. 29. Two-dimensional premultiplied spectra of the viscous dissipation, (a), (d), (g) $k_x k_z E_{\rho_{uu}}^{\varepsilon_k^+}$, (b), (e), (h) $k_x k_z E_{\rho_{vv}}^{\varepsilon_k^+}$, and (c), (f), (i) $k_x k_z E_{\rho_{ww}}^{\varepsilon_k^+}$, at $y^+ = 15, 100$, and 200 , in the hypersonic turbulent boundary layers under three wall conditions. Legends refer to Fig. 5.

4. Heat conduction

The two-dimensional premultiplied spectra of the heat conduction are plotted in Fig. 31. In the inner region ($y^+ = 15$), the spectral peak of $k_x k_z E_{\rho\phi\phi}^{Q^+}$ locates at $(\lambda_x^+, \lambda_z^+) \approx (140, 60)$ in the adiabatic turbulent boundary layer (at $T_w/T_r = 1$), and the action of heat conduction can be sprayed to very small spanwise scales. When the wall is cooled, the shape and orientation of the spectral distribution are maintained; nevertheless larger streamwise- and spanwise-wavelength structures are found to dominate the contribution of heat conduction.

At $y^+ = 100$ and 200 shown in panels (b) and (c), the spectral peaks are unexpectedly observed at smaller scales than those at $y^+ = 15$. This is quite different from the spectra of TIE production, that large amounts of energy are carried by the larger-scale motions in the outer region. The effects of wall temperature on the energy spectra are apparent, particularly at small scales, even far away

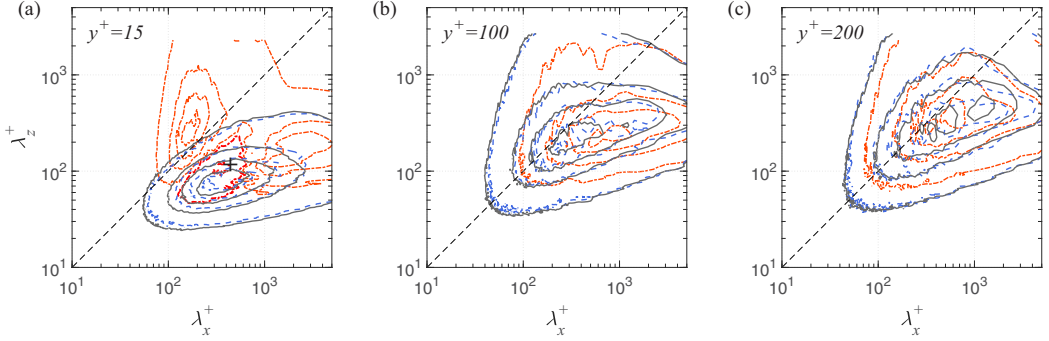


FIG. 30. Two-dimensional premultiplied spectra of the TIE production $k_x k_z E_{\rho\phi\phi}^{Pe+}$ at (a) $y^+ = 15$, (b) $y^+ = 100$, and (c) $y^+ = 200$, in the hypersonic turbulent boundary layers under three wall conditions. Legends refer to Fig. 5, with the contour lines specially denoting 0.05, 0.3, 0.55, and 0.8 of their maximum, moving inward. The red dashed line in Fig. 30(a) denotes -0.05 and -0.3 of the maximum from outside to inside for the *cold2* case.

from the wall. Therefore it is conjectured that the wall-temperature effects on the energy evolution exist throughout the boundary layer, via modifying the small-scale motions primarily. In addition, the isotropic behavior of heat conduction at $y^+ = 100$ is specifically more evident than that of the aforementioned TKE budgets. This is directly associated with the thermal structures, which spread more significantly in the spanwise direction relative to their streamwise elongation than the dynamical structures, at off-wall positions [13].

5. Turbulent convection of turbulence internal energy among scales

Figure 32 shows the two-dimensional spectra of interscale TIE transport at $y^+ = 15$ and 100. Note that in the two-dimensional space, the structure scale λ^+ is determined by both streamwise and spanwise wavelength, as $\lambda^+ = \sqrt{\lambda_x^{+2} + \lambda_z^{+2}}$, which is marked by the dotted lines in Fig. 32. As displayed in panels (a)–(c), the energy donor region is well aligned with the two-dimensional spectra of the TIE production in Fig. 30(a), reconfirming that the interscale transport is capable to redistribute the energy production from the streamwise-elongated modes. On the other hand, the inverse transfer is apparent in the spanwise-elongated region, at $y^+ = 15$. Its mechanism was tentatively explained by Lee and Moser [36], that the transfer from small to large scales is possibly

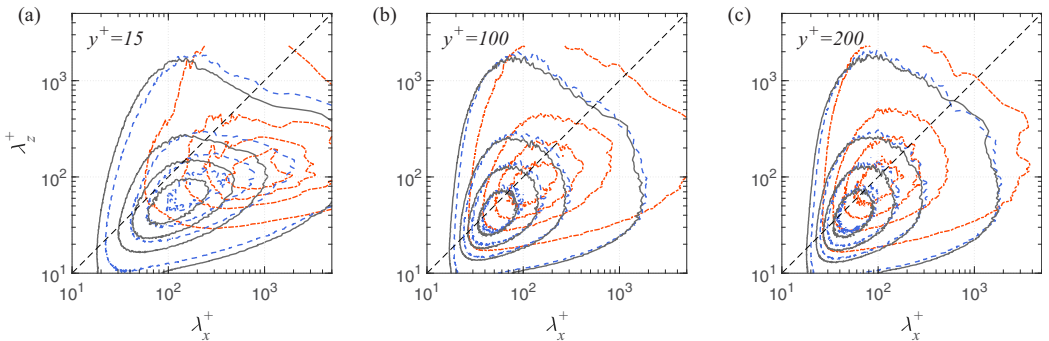


FIG. 31. Two-dimensional premultiplied spectra of the heat conduction $k_x k_z E_{\rho\phi\phi}^{Q+}$ at (a) $y^+ = 15$, (b) $y^+ = 100$, and (c) $y^+ = 200$ in the hypersonic turbulent boundary layers under three wall conditions. Legends refer to Fig. 5.

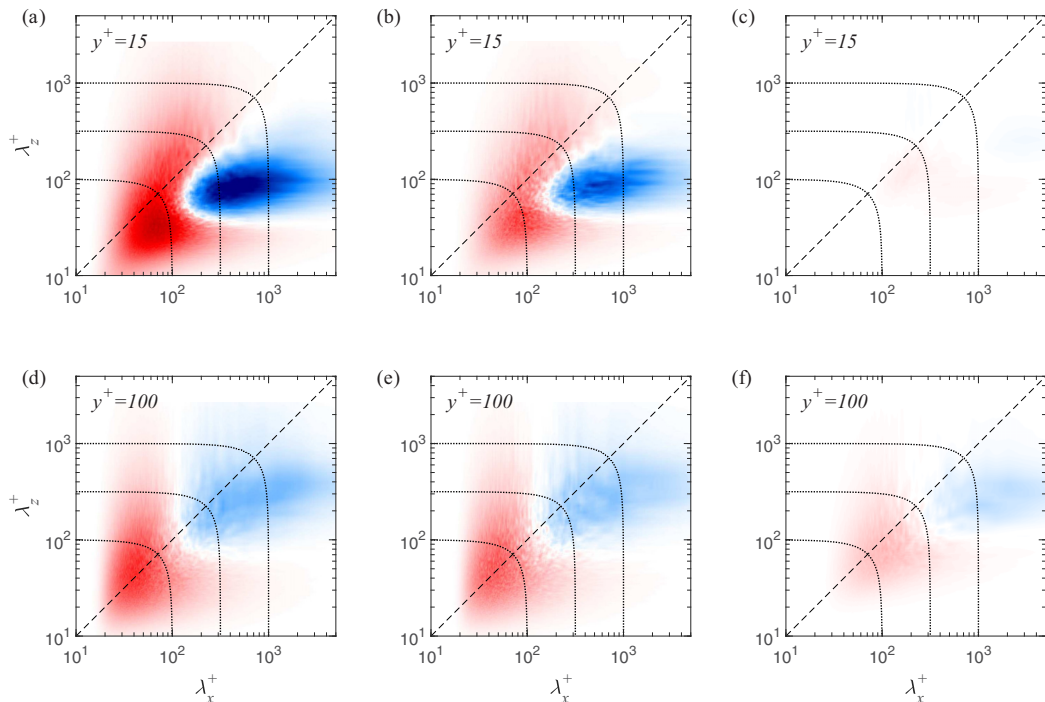


FIG. 32. Two-dimensional premultiplied spectra of the turbulent convection of TIE among scales, $k_x k_z E_{\rho\phi\phi}^{D_{r,\parallel}+}$, in the hypersonic turbulent boundary layers at (a), (d) $T_w/T_r = 1.0$, (b), (e) $T_w/T_r = 0.76$, and (c), (f) $T_w/T_r = 0.25$ at $y^+ = 15$ and 100. The ranges of color bar in these figures are the same, with blue to red denoting negative to positive values $[-0.002, 0.002]$. The outermost dotted line denotes $\lambda^+ = 1000$ and decreases with a factor of $1/\sqrt{10}$ for each dotted line moving inward.

due to the nonlinear interaction of outer-layer large-scale motions and the inner-layer small scales, as the receipt larger-scale region in $k_x k_z E_{\rho\phi\phi}^{D_{r,\parallel}+}$ coincides with the receipt region in $k_x k_z E_{\rho\phi\phi}^{D_{r,\perp}+}$. This phenomenon is also observed in the present results but not repeatedly shown. Away from the wall, this peculiar phenomenon vanishes. In addition to the redistribution across scales, at a given scale λ^+ , energy transfer is also observed towards motions with a different orientation of wavelength [73], e.g., from streamwise-oriented motions to spanwise-oriented ones. The strong wall cooling attenuates the turbulent energy transport and its spectra are hard to identify in the maps of panels (c) and (f), as also suggested by Fig. 27.

-
- [1] M. V. Morkovin, Effects of compressibility on turbulent flows, in *Mécanique de la Turbulence*, edited by A. Favre (1962), pp. 367–380.
- [2] P. Bradshaw, Compressible turbulent shear layers, *Annu. Rev. Fluid Mech.* **9**, 33 (1977).
- [3] E. F. Spina, A. J. Smits, and S. K. Robinson, The physics of supersonic turbulent boundary layers, *Annu. Rev. Fluid Mech.* **26**, 287 (1994).
- [4] S. Sarkar, The stabilizing effect of compressibility in turbulent shear flow, *J. Fluid Mech.* **282**, 163 (1995).
- [5] S. K. Lele, Compressibility effects on turbulence, *Annu. Rev. Fluid Mech.* **26**, 211 (1994).
- [6] A. W. Vreman, N. D. Sandham, and K. H. Luo, Compressible mixing layer growth rate and turbulence characteristics, *J. Fluid Mech.* **320**, 235 (1996).

- [7] S. Pirozzoli, F. Grasso, and T. B. Gatski, Direct numerical simulation and analysis of a spatially evolving supersonic turbulent boundary layer at $M = 2.25$, *Phys. Fluids* **16**, 530 (2004).
- [8] S. Pirozzoli and F. Grasso, Direct numerical simulations of isotropic compressible turbulence: Influence of compressibility on dynamics and structures, *Phys. Fluids* **16**, 4386 (2004).
- [9] A. J. Smits and J. P. Dussauge, Boundary layer mean-flow behavior, in *Turbulent Shear Layers in Supersonic Flow* (Springer, New York, 2006), pp. 179–215.
- [10] S. Pirozzoli, M. Bernardini, and F. Grasso, Characterization of coherent vortical structures in a supersonic turbulent boundary layer, *J. Fluid Mech.* **613**, 205 (2008).
- [11] L. Duan, I. Beekman, and M. P. Martin, Direct numerical simulation of hypersonic turbulent boundary layers, Part 2. Effect of wall temperature, *J. Fluid Mech.* **655**, 419 (2010).
- [12] L. Duan, I. Beekman, and M. P. Martin, Direct numerical simulation of hypersonic turbulent boundary layers, Part 3. Effect of Mach number, *J. Fluid Mech.* **672**, 245 (2011).
- [13] S. Pirozzoli and M. Bernardini, Turbulence in supersonic boundary layers at moderate Reynolds number, *J. Fluid Mech.* **688**, 120 (2011).
- [14] M. Bernardini and S. Pirozzoli, Wall pressure fluctuations beneath supersonic turbulent boundary layers, *Phys. Fluids* **23**, 085102 (2011).
- [15] Y.-S. Zhang, W.-T. Bi, F. Hussain, X.-L. Li, and Z.-S. She, Mach-Number-Invariant Mean-Velocity Profile of Compressible Turbulent Boundary Layers, *Phys. Rev. Lett.* **109**, 054502 (2012).
- [16] S. Pirozzoli and M. Bernardini, Probing high-Reynolds-number effects in numerical boundary layers, *Phys. Fluids* **25**, 021704 (2013).
- [17] Y.-B. Chu, Y.-Q. Zhuang, and X.-Y. Lu, Effect of wall temperature on hypersonic turbulent boundary layer, *J. Turbul.* **14**, 37 (2013).
- [18] A. Hadjadj, O. Ben-Nasr, M. S. Shadloo, and A. Chaudhuri, Effect of wall temperature in supersonic turbulent boundary layers: A numerical study, *Int. J. Heat Fluid Flow* **81**, 426 (2015).
- [19] D. Modesti and S. Pirozzoli, Reynolds and Mach number effects in compressible turbulent channel flow, *Int. J. Heat Fluid Flow* **59**, 33 (2016).
- [20] J.-C. Wang, M.-P. Wan, S. Chen, and S.-Y. Chen, Kinetic energy transfer in compressible isotropic turbulence, *J. Fluid Mech.* **841**, 581 (2018).
- [21] C. Wenzel, B. Selent, Ma. Kloker, and U. Rist, DNS of compressible turbulent boundary layers and assessment of data/scaling-law quality, *J. Fluid Mech.* **842**, 428 (2018).
- [22] D. Li, A. Peyvan, Z. Ghiasi, J. Komperda, and F. Mashayek, Compressibility effects on energy exchange mechanisms in a spatially developing plane free shear layer, *J. Fluid Mech.* **910**, A9 (2021).
- [23] C. Wenzel, T. Gibis, and M. Kloker, About the influences of compressibility, heat transfer and pressure gradients in compressible turbulent boundary layers, *J. Fluid Mech.* **930**, A1 (2022).
- [24] X. Liang and X.-L. Li, Direct numerical simulation on Mach number and wall temperature effects in the turbulent flows of flat-plate boundary layer, *Commun. Comput. Phys.* **17**, 189 (2015).
- [25] C. Zhang, L. Duan, and M. M. Choudhari, Effect of wall cooling on boundary-layer-induced pressure fluctuations at Mach 6, *J. Fluid Mech.* **822**, 5 (2017).
- [26] C. Zhang, L. Duan, and M. M. Choudhari, Direct numerical simulation database for supersonic and hypersonic turbulent boundary layers, *AIAA J.* **56**, 4297 (2018).
- [27] M. Yu and C.-X. Xu, Compressibility effects on hypersonic turbulent channel flow with cold walls, *Phys. Fluids* **33**, 075106 (2021).
- [28] D.-H. Xu, J.-C. Wang, M.-P. Wan, C.-P. Yu, X.-L. Li, and S.-Y. Chen, Effect of wall temperature on the kinetic energy transfer in a hypersonic turbulent boundary layer, *J. Fluid Mech.* **929**, A33 (2021).
- [29] E. R. van Driest, Turbulent boundary layer in compressible fluids, *J. Aeronaut. Sci.* **18**, 145 (1951).
- [30] Y.-S. Zhang, W.-T. Bi, F. Hussain, and Z.-S. She, A generalized Reynolds analogy for compressible wall-bounded turbulent flows, *J. Fluid Mech.* **739**, 392 (2014).
- [31] A. Trettel and J. Larsson, Mean velocity scaling for compressible wall turbulence with heat transfer, *Phys. Fluids* **28**, 026102 (2016).
- [32] M. S. Shadloo, A. Hadjadj, and F. Hussain, Temperature-invariant scaling for compressible turbulent boundary layers with wall heat transfer, *Heat Transfer Eng.* **39**, 923 (2018).

- [33] K. P. Griffin, L. Fu, and P. Moin, Velocity transformation for compressible wall-bounded turbulent flows with and without heat transfer, *Proc. Natl. Acad. Sci. USA* **118**, e2111144118 (2021).
- [34] M. S. Shadloo, A. Hadjadj, and F. Hussain, Statistical behavior of supersonic turbulent boundary layers with heat transfer at $M_\infty = 2$, *Int. J. Heat Fluid Flow* **53**, 113 (2015).
- [35] D.-H. Xu, J.-C. Wang, M.-P. Wan, C.-P. Yu, X.-L. Li, and S.-Y. Chen, Compressibility effect in hypersonic boundary layer with isothermal wall condition, *Phys. Rev. Fluids* **6**, 054609 (2021).
- [36] M. Lee and R. D. Moser, Spectral analysis of the budget equation in turbulent channel flows at high Reynolds number, *J. Fluid Mech.* **860**, 886 (2019).
- [37] C. I. Chan, P. Schlatter, and R. C. Chin, Interscale transport mechanisms in turbulent boundary layers, *J. Fluid Mech.* **921**, A13 (2021).
- [38] D. H. Richter, Turbulence modification by inertial particles and its influence on the spectral energy budget in planar Couette flow, *Phys. Fluids* **27**, 063304 (2015).
- [39] F. Aulery, D. Dupuy, A. Toutant, F. Bataille, and Y. Zhou, Spectral analysis of turbulence in anisothermal channel flows, *Comput. Fluids* **151**, 115 (2017).
- [40] A. Mittal and S. S. Girimaji, Mathematical framework for analysis of internal energy dynamics and spectral distribution in compressible turbulent flows, *Phys. Rev. Fluids* **4**, 042601(R) (2019).
- [41] S. Kida and S. A. Orszag, Energy and spectral dynamics in decaying compressible turbulence, *J. Sci. Comput.* **7**, 1 (1992).
- [42] D. S. Praturi and S. S. Girimaji, Effect of pressure-dilatation on energy spectrum evolution in compressible turbulence, *Phys. Fluids* **31**, 055114 (2019).
- [43] T. T. Clark, Two-point evolution equations for incompressible variable density turbulence, [arXiv:2011.03345](https://arxiv.org/abs/2011.03345).
- [44] S. Arun, A. Sameen, B. Srinivasan, and S. S. Girimaji, Scale-space energy density function transport equation for compressible inhomogeneous turbulent flows, *J. Fluid Mech.* **920**, A31 (2021).
- [45] T. T. Clark and P. B. Spitz, Two-point correlation equations for variable density turbulence, Technical Report LA-12671-MS, Los Alamos National Laboratory, p. 6, 1995.
- [46] H. Miura and S. Kida, Acoustic energy exchange in compressible turbulence, *Phys. Fluids* **7**, 1732 (1995).
- [47] Y.-T. Fan, W.-P. Li, and S. Pirozzoli, Energy exchanges in hypersonic flows, *Phys. Rev. Fluids* **7**, L092601 (2022).
- [48] M. Bernardini, D. Modesti, F. Salvadore, and S. Pirozzoli, STREAmS: A high-fidelity accelerated solver for direct numerical simulation of compressible turbulent flows, *Comput. Phys. Commun.* **263**, 107906 (2021).
- [49] G.-S. Jiang and C.-W. Shu, Efficient implementation of weighted ENO schemes, *J. Comput. Phys.* **126**, 202 (1996).
- [50] P. R. Spalart, R. D. Moser, and M. M. Rogers, Spectral methods for the Navier-Stokes equations with one infinite and two periodic directions, *J. Comput. Phys.* **96**, 297 (1991).
- [51] T. J. Poinso and S. K. Lele, Boundary conditions for direct simulations of compressible viscous flows, *J. Comput. Phys.* **101**, 104 (1992).
- [52] M. Klein, A. Sadiki, and J. Janicka, A digital filter based generation of inflow data for spatially developing direct numerical or large eddy simulations, *J. Comput. Phys.* **186**, 652 (2003).
- [53] M. Lagha, J. Kim, J. D. Eldredge, and X. Zhong, A numerical study of compressible turbulent boundary layers, *Phys. Fluids* **23**, 015106 (2011).
- [54] J. Huang, L. Duan, and M. M. Choudhari, Direct numerical simulation of hypersonic turbulent boundary layers: Effect of spatial evolution and Reynolds number, *J. Fluid Mech.* **937**, A3 (2022).
- [55] M. Lee and R. D. Moser, Direct numerical simulation of turbulent channel flow up to $Re_\tau \approx 5200$, *J. Fluid Mech.* **774**, 395 (2015).
- [56] Y. Hwang, Statistical structure of self-sustaining attached eddies in turbulent channel flow, *J. Fluid Mech.* **767**, 254 (2015).
- [57] A. A. Townsend, *The Structure of Turbulent Shear Flow* (Cambridge University Press, Cambridge, UK, 1976).
- [58] C. Brun, M. P. Boiarciuc, M. Haberkorn, and P. Comte, Large eddy simulation of compressible channel flow, *Theor. Comput. Fluid Dyn.* **22**, 189 (2008).

- [59] Y. Hwang, Near-wall turbulent fluctuations in the absence of wide outer motions, *J. Fluid Mech.* **723**, 264 (2013).
- [60] N. Hutchins and I. Marusic, Large-scale influences in near-wall turbulence, *Philos. Trans. R. Soc. London, Ser. A* **365**, 647 (2007).
- [61] B. J. Balakumar and R. J. Adrian, Large- and very-large-scale motions in channel and boundary-layer flows, *Philos. Trans. R. Soc. A* **365**, 665 (2007).
- [62] J. Lee and H. Sung, Very-large-scale motions in a turbulent boundary layer, *J. Fluid Mech.* **673**, 80 (2011).
- [63] J. Kim, P. Moin, and R. Moser, Turbulence statistics in fully developed channel flow at low Reynolds number, *J. Fluid Mech.* **177**, 133 (1987).
- [64] B. Ganapathisubramani, N. Hutchins, W. T. Hambleton, E. K. Longmire, and I. Marusic, Investigation of large-scale coherence in a turbulent boundary layer using two-point correlations, *J. Fluid Mech.* **524**, 57 (2005).
- [65] A. Cimarelli, E. De Angelis, and C. M. Casciola, Paths of energy in turbulent channel flows, *J. Fluid Mech.* **715**, 436 (2013).
- [66] M. de Giovanetti, Y. Hwang, and H. Choi, Skin-friction generation by attached eddies in turbulent channel flow, *J. Fluid Mech.* **808**, 511 (2016).
- [67] S. B. Pope, *Turbulent Flows* (Cambridge University Press, Cambridge, UK, 2000).
- [68] D. Gatti, A. Chiarini, A. Cimarelli, and M. Quadrio, Structure function tensor equations in inhomogeneous turbulence, *J. Fluid Mech.* **898**, A5 (2020).
- [69] R. Mathis, N. Hutchins, and I. Marusic, Large-scale amplitude modulation of the small-scale structures in turbulent boundary layers, *J. Fluid Mech.* **628**, 311 (2009).
- [70] I. Marusic, R. Mathis, and N. Hutchins, Predictive model for wall-bounded turbulent flow, *Science* **329**, 193 (2010).
- [71] J. M. Hamilton, J. Kim, and F. Waleffe, Regeneration mechanisms of near-wall turbulence structures, *J. Fluid Mech.* **287**, 317 (1995).
- [72] T. Kawata and P. H. Alfredsson, Inverse Interscale Transport of the Reynolds Shear Stress in Plane Couette Turbulence, *Phys. Rev. Lett.* **120**, 244501 (2018).
- [73] S. Symon, S. J. Illingworth, and I. Marusic, Energy transfer in turbulent channel flows and implications for resolvent modelling, *J. Fluid Mech.* **911**, A3 (2021).